UNIVERSITY OF TWENTE.

**Faculty of Electrical Engineering,
Mathematics & Computer Science**

Interference Robust Spatial Multiplexing

Jippe R. Rossen

M.Sc. Thesis

June 19, 2018

Supervisors:
Dr. ir. A.B.J. Kokkeler
Dr. ing. E.A.M. Klumperink
Dr. ing. D.M. Ziener
M. Abbasi Alaei M.Sc.

Computer Architecture for
Embedded Systems (CAES) group
Faculty of Electrical Engineering,
Mathematics and Computer Science
University of Twente

Abstract

This project focuses on the practical application of techniques regarding spatial multiplexing. Spatial multiplexing is implemented by estimating the channel matrix using a least squares approximation. The obtained channel matrix is decomposed using a singular value decomposition. The resulting singular values and singular vectors for various scenarios are related back to the principles of spatial multiplexing.

A simulation environment is created to make the techniques more insightful and to provide a baseline performance on what to expect from practical scenarios. Using standard building materials and basic RF equipment, a setup is constructed to do practical experiments. Experiments are carried out to characterize the behavior of the transceiver system in both a controlled environment as well as in practical scenario's.

Another aspect of this research is the robustness of the system against interference. Using Multiple Signal Classification (MUSIC) a profile is made from possible interferers within the surroundings. This profile is then used to create a spatial filter which can be used to suppress the influence of the interferer. This technique is implemented to view the performance of such a filter for both simulations as well as a practical scenario.

Acknowledgements

I would like to thank my supervisors André, Eric and Massoud for their guidance, their insights and the useful discussions I have had with all of them. I am also especially appreciative for their patience and allowing me the time to do countless other activities in parallel to my graduation project.

I would also like to express my thanks to Henk de Vries for providing various pieces of lab equipment and his advise on how to get the best lab results.

I am grateful for the support I received from Robert Vogt-Ardatjew. His knowledge on the specifics of anechoic chambers has proven most helpful and has contributed to this research a lot.

I would like to thank all people of the research group of Computer Architecture for Embedded Systems for the great time I have had whilst working on my graduation project. A special thanks I would like to give to Hendrik Folmer and Robert de Groote for putting up with me in an office. It has provided a very nice environment for me to work in and I had great time with you guys.

Lastly, I would like to thank my family for their unconditional love and support during my entire education.

Contents

Chapter 1

Introduction

With the progress in processing power in digital communication systems, many new techniques to increase performance have been invented. There remain, however, a few complications in such systems. Multi path fading causes systems to introduce self interference when communication signals in the form of electromagnetic signals are reflected by objects along the transmission path. These reflections cause delayed instances of the original signal on the receiver of the communication line. These delayed instances add to other interference signals and deteriorate the Signal to Noise Ratio (SNR).

Also, as the number of communication systems increase, the allocated frequencies in the electromagnetic spectrum become more crowded. Especially in dense urban areas, local wireless networks interfere with one another to such an extent that a substantial decrease in performance is perceived.

By employing Direction of Arrival (DOA) estimation techniques it is possible to determine the angle of incidence of incoming signals. The receiver can be tuned to only receive signals from a particular direction, which effectively cancels undesired signals from other directions, which is called beamforming. There has been a vast amount of research on this topic ([1],[2]). When the transmitter is also equipped with an array of antennas, also the transmitted beamfront can be steered. By using superposition, multiple signals can be transmitted in multiple directions. When these techniques are used at the same time, many different combinations of transmit and receive angles are possible, which will result in many different channels.

When the receiver antenna array has M elements and the transmitter array has N antennas, each of the antenna combinations between transmitter and receiver has its own transfer characteristics. A channel matrix can be constructed which consists of M by N elements, which characterizes the transfer between each individual antenna pair. One of the aspects of this project is to determine and describe how this matrix corresponds to the spatial transmission paths and how these are affected by neighboring systems. Evaluations will be performed on how spatial multiplexing can be applied in a robust way to limit the effects of interference from these neighboring systems. Simulations will be performed in combination with real physical evaluations to validate proposed techniques.

Concluding, the research goals of this project are:

1. Explore existing literature on channel estimation, Singular Value Decomposition and/or Principal Component Analysis in the context of spatial multiplexing.

2. Use an existing channel estimation algorithm to determine the channel matrix.

3. Find for 4x4 Multiple Input Multiple Output (MIMO) channels the optimal spatial transmission paths.
4. Investigate how the (spatial transmission) channels are affected by- and affect neighboring communication systems and how this can be reduced by looking at the interference footprint.

Chapter 2

Transmission Techniques and Characteristics

2.1 Global outline

To address the research goals, a simple use case will be introduced to indicate the topics on which this project focuses. This arbitrary case will then be utilized to elaborate on more in-depth concepts of the tasks at hand. First this will be explored using Matlab simulations, after which it will be tested in real scenarios using actual hardware.

Figure 2.1 shows an arbitrary environment in which a communication system is employed of two antennas (A_1, A_2), both capable of transmitting and receiving. For simplicity and clearity, suppose that A_1 is only used for transmission and A_2 is only used for receiving. As both A_1 and A_2 have only a single transmitter and a single receiver, this system can be considered as a Single Input Single Output (SISO) system.

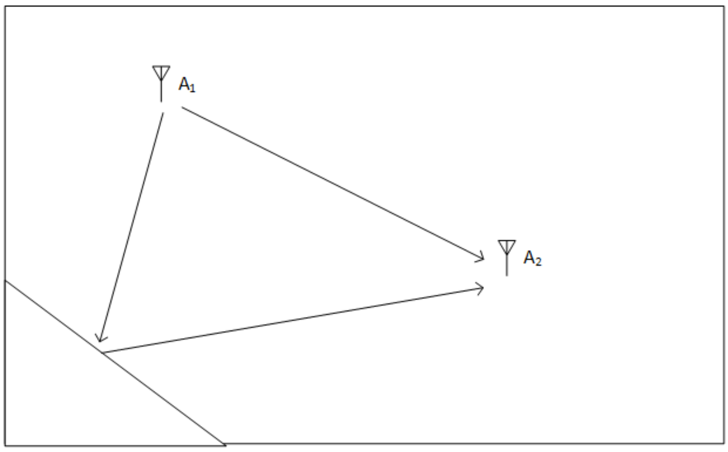

Figure 2.1: Communication system in an arbitrary environment.

As soon as A_1 starts transmitting data, Electromagnetic (EM)-waves start propagating through the room. As indicated in figure 2.1 multiple paths will exist between a sender and a receiver. Choosing an arbitrary sampling moment, multiple signals will be present at the receiver. In traditional communication techniques, the dominant signal is assumed to be the desired signal. All other impinging signals are reflections from the signal that was transmitted in an earlier point in time or interference. Note that in the case of a stronger interferer which

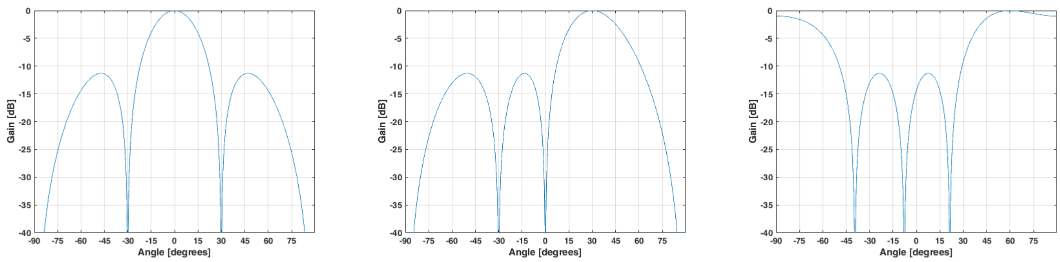

(a) 0 degrees (b) 30 degrees (c) 60 degrees

Figure 2.2: Directional sensitivity for specific steering angles of an antenna array.

occupies the same frequency band, the desired signal is lost.

In figure 2.1 the transmitter and the receiver are single antennas. If now these antennas are replaced by arrays, the linear phased-array setup of figure 2.3 is created. Both A_1 and A_2 are now equipped with four antennas each ($n_r, n_t = 4$), making it a MIMO system. By adding delays (phase shifts) to the received signals and summing the results, the antenna can be made directional. Figures 2.2a through figure 2.2c show the resulting gain of the array against the Angle of Incidence (AoI) when the receiver array is set for a steering angle of 0°, 30°and 60°. This makes beamforming quite effective in the suppression of unwanted signals from angles of no interest. Especially the concept of null steering can be very effective to suppress known interferers[3]. In the end, however, all it does is raising the SNR of a transmission link.

Shannon's theorem for link capacity (equation 2.1) dictates that the increase of SNR can be used to improve the channel's capacity[4]. Because of the logarithmic nature of this equation, doubling the SNR will provide only a very limited increase in the data rate. By applying spatial multiplexing this logarithmic relation can be avoided as the spectral efficiency can be increased linearly with the number of paths.

$$C = B \cdot log_2(1 + \frac{S}{N}) \tag{2.1}$$

2.2 Steering vectors

A linear phased array can be made sensitive to a certain angle by employing a so called steering vector. This vector, which has the same dimension as the number of antennas in the array, contains a phase rotation and a gain for each separate antenna. These phase rotations cause the received signals on the antennas to be in the same phase resulting in constructive interference for the angle of the steering vector and destructive interference for other angles.

By creating a wavefront and applying the steering vector to it, the gain for the steering vector can be determined for the angle of incidence of the wavefront. By doing this for every angle of incidence and applying the steering vector to each of these wavefronts, an angular sensitivity plot can be made. In figure 2.2 this has been done for artificial steering vectors for angles of 0°, 30°and 60° for a four antenna phased array.

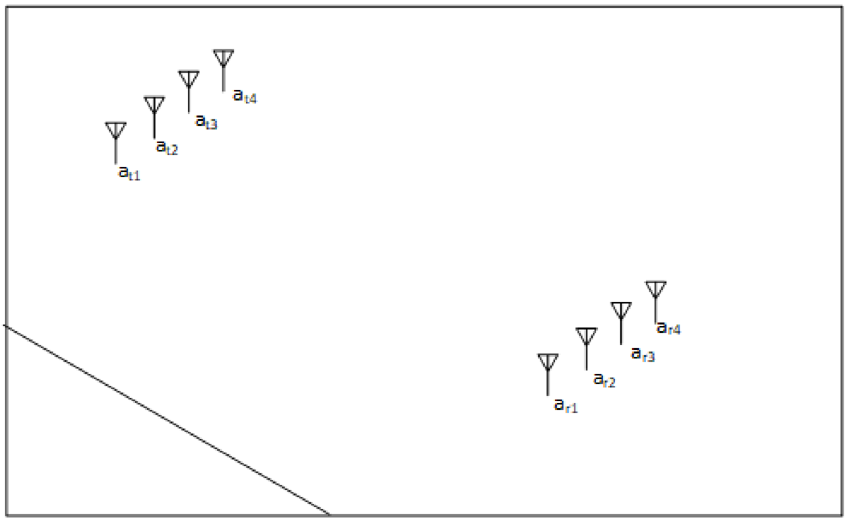

Figure 2.3: Communication system with linear phased array antennas on both the receiver as the transmitter side.

2.3 Multipaths & spatial multiplexing

In figure 2.4, the simple model of figure 2.3 is extended with the spatial transmission paths possible in this environment. The direct path between both arrays is still present. However, also a secondary path is shown which originates by a reflection on a wall. The first signal has an AoI of 0°, where the second has an AoI of -45°. Assuming that it is possible to mathematically separate and isolate these signals, it should be possible to send two different streams of data over the two individual channels. The technique of transmitting multiple streams of the same frequency in the same space at the same time is known as spatial multiplexing.

There are some complications about using spatial multiplexing. When signals are broadcast at the same time at the same frequency, they start interfering with one another. The receiver array can be made sensitive to a certain direction, but will generally not be able to completely cancel signals from other angles. This interference has a direct impact on the SNR. Another issue is that the sensitivity of the array to a certain direction is limited by the number of antennas in the array. For the array to be able to cancel signals from unwanted directions they should have a large enough angular separation to prevent them from interfering too much with one another.

2.4 Channel characteristics

To identify suitable transmission paths, the channel has to be characterized. A model has to be made that describes how the transmitted signals of each antenna are subjected to alterations in phase and gain. This is done by determining the channel transmission matrix **H**, which is also known as the Channel State Information (CSI).

2.4.1 The channel matrix

The matrix **H** has dimensions n_r by n_t which are determined by the number of antennas at the receiver and transmitter. Each of the values in this matrix gives a representation between both

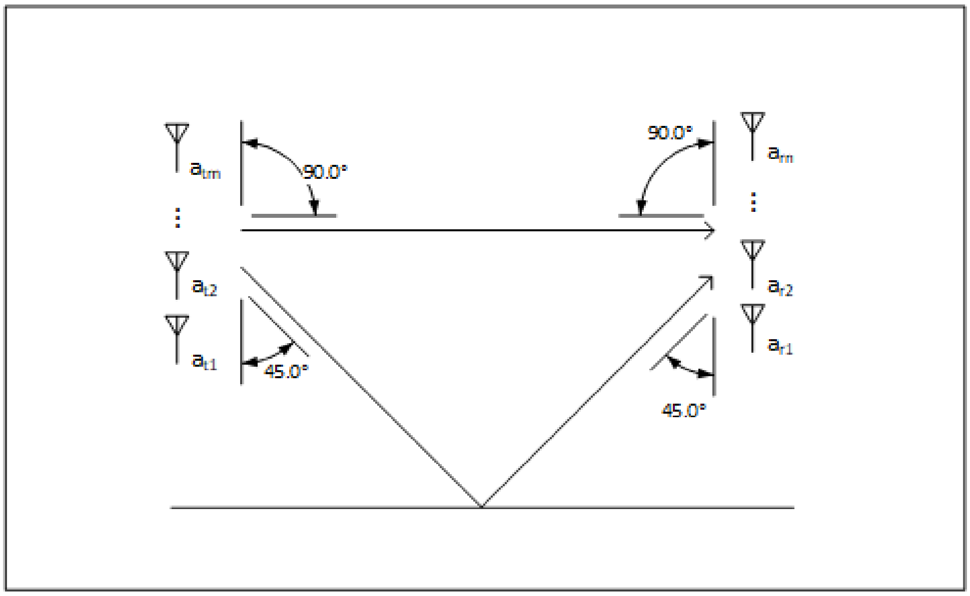

Figure 2.4: Communication system with a direct path and a reflection path.

the gain (loss) and the phase of each possible transmit and receive antenna pair. The received signal can then be described by:

$$\mathbf{y} = \mathbf{H}\mathbf{x} + \mathbf{w} \tag{2.2}$$

In which $\mathbf{x}$ is a vector containing the transmitted signal by $a_{t1}..a_{tm}$ and $\mathbf{y}$ is a vector containing the signals received by antennas $a_{r1}..a_{rn}$ (which are defined in figure 2.4). $\mathbf{H}$ is a m by n matrix containing the transfer function of every possible antenna pair in the system. The values of $\mathbf{H}$ are complex, as they need to contain both the amplitude and the phase relation. In this equation $\mathbf{w}$ denotes the noise that is present in the system. It is assumed that the noise is white Gaussian in nature.

2.4.2 Estimation of a channel

So far it was assumed that $\mathbf{H}$ was known to both receiver and transmitter. In any realistic scenario this is not the case, thus it has to be estimated. To do this a training sequence is required. The training sequence is known to both the receiver and the transmitter and is used to determine the transfer function between all possible combination pairs of transmitter and receiver antennas. A lot of research has been done on the topic of optimal training sequences for specific systems and environments [5]. As the proposed setup is a stand-alone communication system in an arbitrary environment, the transfer function and noise distributions are unknown. Therefore a least squares estimation is best suited to find the $\mathbf{H}$ matrix[6, chapter 3], see equation 2.3.

$$\mathbf{H}_{\mathbf{LS-estimate}} = \mathbf{YP}^*(\mathbf{PP}^*)^{-1} \tag{2.3}$$

In this equation is $\mathbf{Y}$ denotes the received samples. It is a n-by-k matrix in which n is the number of antennas in the receiver array and k the number of training samples. $\mathbf{P}$ is the training set consisting of k samples for the m transmit antennas. The operator * denotes the Hermetian-, or complex conjugate transpose. $\mathbf{P}$ is chosen such that $\mathbf{PP}^*$ is a m-by-m identity matrix. The length of the training sequence can be varied. In case of white Gaussian noise the variance in the estimation can be decreased by a factor q when the length of the training

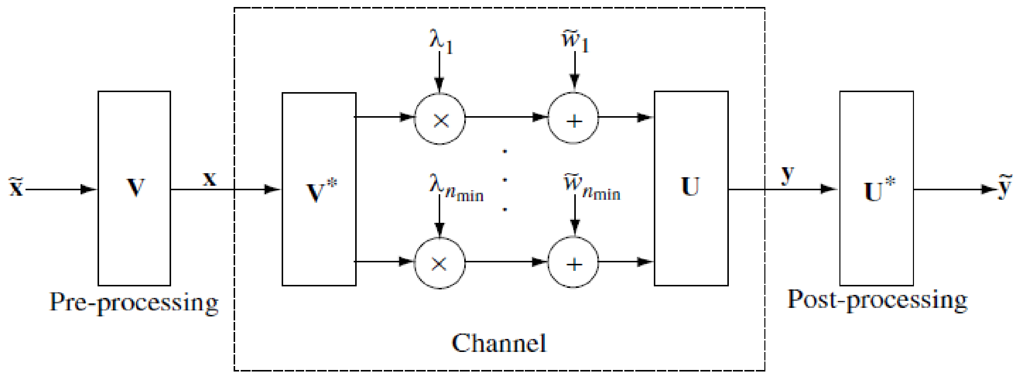

Figure 2.5: Graphic reepresentation of decomposing the channel matrix into multiple SISO channels. The and $\mathbf{V}^*$ matrix maps the signals to eigenmodes and the $\mathbf{U}$ matrix maps them back to the original coordinate frame. [10]

sequence is multiplied by a factor q.

2.4.3 Multiplexing capability

The effectiveness of spatial multiplexing is strongly dependent on the surroundings. It will be assumed that the channel matrix $\mathbf{H}$ is time-invariant[1]. In this section also the assumption is taken that the channel matrix is known to both transmitter and receiver. To understand how the characteristics of $\mathbf{H}$ determine the spatial multiplexing capabilities of a wireless channel, a closer look at the capacity of the channel is taken.

In equation 2.2 the relation between a transmitted signal, the received signal and the transmission matrix $\mathbf{H}$ was introduced. Linear algebra shows that every matrix can be decomposed into three other matrices, a rotation matrix, a scaling matrix and another rotation matrix, which is called a Singular Value Decomposition (SVD)[7, Chapter 3]. This operation can be interpreted as two coordinate transformations and a simple scaling operation. The coordinate transformations effectively map the MIMO channel into multiple parallel SISO channels, which can be called eigenmodes. For each of these channels Shannon's link capacity theorem holds. This also shows how spatial multiplexing can improve the link capacity. Equation 2.4 shows this decomposition mathematically and figure 2.5 shows how the result of this operation can be interpreted as multiple SISO channels.[8, Chapter 7][9]

$$\mathbf{H} = \mathbf{U}\mathbf{\Lambda}\mathbf{V}^* \tag{2.4}$$

In equation 2.4, $\mathbf{U}$ and $\mathbf{V}^*$ are both unitary matrices ($\mathbf{M}^{-1} = \mathbf{M}^*$) giving them the property that $\mathbf{M}\mathbf{M}^* = \mathbf{M}^*\mathbf{M} = \mathbf{I}$, with I being the identity matrix. The columns of a unitary matrix form an orthonormal set. The vectors of the $\mathbf{U}$ matrix are also known as the left singular vectors and the ones from the $\mathbf{V}^*$ matrix the right singular vectors.

Figure 2.5 shows that the vectors of these matrices are used for coordinate transformations at both the receiver as the transmitter. These transformations map the signals onto the eigen-

[1]In real life scenarios this may or may not be the case, depending on the environment and for the time span the estimated matrix is assumed to be valid.

modes and map them back to the original coordinate frame. As the eigenmodes are in this case spatial paths, the vectors of these matrices act as steering vectors for the system.

$\mathbf{\Lambda}$ is a rectangular matrix with on its diagonal the real-valued singular values ($\lambda_1 \geq \lambda_2 \geq \lambda_n$) of the matrix $\mathbf{H}$ and all off-diagonal elements are zero (see 2.5). The dimensions of $\mathbf{\Lambda}$ are dependent on the number of antennas in both the transmitting (n_t) as the receiving array (n_r). $\mathbf{\Lambda}$ may therefore not be square.

$$\mathbf{\Lambda} = \begin{bmatrix} \lambda_1 & 0 & \dots & 0 \\ 0 & \lambda_2 & \dots & 0 \\ \vdots & \vdots & \ddots & \vdots \\ 0 & 0 & \dots & \lambda_n \end{bmatrix} \tag{2.5}$$

These singular values indicate the suitability of an environment for spatial multiplexing. The singular values each correspond to an eigenmode and are ordered from strongest to weakest. For a perfect scenario all these singular values would have the same value. In that case the power could be distributed equally giving the maximum link capacity. This scenario actually only exists when the eigenmodes are guided from transmitter to receiver through cables, which isolates each eigenmode completely from one another.

For a wireless system the signals do interfere with one another causing the singular values to drop off. The lower a singular value is, the weaker the corresponding eigenmode will be. The singular values should be assessed simultaneously with the SNR to see whether it makes sense to allocate power to a specific eigenmode at the SNR of that eigenmode. This allocation of power is generally done using waterfilling techniques. During waterfilling, power is allocated to the eigenmodes to achieve optimal link capacity. As this depends on both the SNR and the singular values, it is difficult to give a general statement on when an eigenmode is suitable for spatial multiplexing.

The number of singular values and eigenmodes are limited by the number of antennas in both the transmission array as the receiving array: $n = min(n_t, n_r)$. This implies that the maximum number of eigenmodes available is equal to the smallest number of antennas in either of the arrays.

2.4.4 Condition number

To determine how many paths are suited for spatial multiplexing, some sort of measure is required. The concept of the condition number can be used for this purpose[11, p100]. The condition number is defined by:

$$CN = \frac{max\lambda_n}{min\lambda_n} \tag{2.6}$$

The condition number only gives a measure on the weakest eigenmode with respect to the strongest eigenmode. The waterfilling techniques could opt to only use the strongest eigenmode or the two strongest eigenmodes. In that sense the condition number is not that useful. It does however give a good indication on how well the channel matrix is conditioned.

As the condition number is just a ratio of the weakest singular value with respect to the strongest singular value, it can be calculated for the other singular values as well. This results in an array of values equal in length to the number of singular values. The first of these is always 1 and the last being always equal to the condition number. These condition ratios will quickly give an indication of the suitability of each eigenmode for spatial multiplexing.

2.5 Synchronization

Up until now it was assumed that only a phase shift was present in the communication line between transmitter and receiver. The fact that the receiver and transmitter are not synchronized does introduce some complications. During sampling the signals are subject to an arbitrary offset in samples. The least squares estimation presented above requires the pilot signal's samples to be aligned with the received signals so this has to be dealt with.

The offset in samples can be determined by performing a cross correlation between the training signals and the received signals[12]. For every transceiver channel pair (for example $a_{t1} - a_{r1}$), the cross correlation operation results in a vector of correlation values between the transmitted signals and the received signals. By summing the magnitudes of the correlations of the individual channels, a vector of combined correlations can be found for the offset between the received signals and the pilot signals. The maximum combined correlation is the assumed offset and is used to synchronize the two signal sets[2].

2.6 Direction of arrival

Although it is not necessary for spatial multiplexing, the DOA algorithm Multiple Signal Classification (MUSIC)[13] can be used to visualize the relation between the angle of incidence and the received power more distinctly. MUSIC works by using the system's noise subspace to find the DOA of the received signals. The subspaces are found by calculating the eigenvalues (**D**) and eigenvectors (**V**) of the co-variance matrix of the received signals. This results in a number of eigenvectors equal to the number of receive antennas. Each of these eigenvectors can be considered a subspace. By choosing how many of these belong to the noise subspace, the number of peaks found by the music algorithm can be controlled. If the noise subspace uses all eigenvectors but one, only a single peak will be detected (the noise subspace is in that case of dimension n-1 and the signal subspace has only a single dimension).

Let $\mathbf{a}(\phi, \mathbf{n})$ be a steering vector consisting of n elements, in which n is the number of antennas in the receiver. This research focuses on the use of linear phased arrays therefore $\mathbf{a}(\phi, \mathbf{n})$ will be defined as is shown in equation 2.7.

$$\mathbf{a}(\phi, \mathbf{n}) = \begin{bmatrix} e^{-i\cdot\omega\cdot\frac{f_{carrier}}{c}\cdot\Delta\cdot 0\cdot sin(\phi)} \\ e^{-i\cdot\omega\cdot\frac{f_{carrier}}{c}\cdot\Delta\cdot 1\cdot sin(\phi)} \\ e^{-i\cdot\omega\cdot\frac{f_{carrier}}{c}\cdot\Delta\cdot 2\cdot sin(\phi)} \\ \vdots \\ e^{-i\cdot\omega\cdot\frac{f_{carrier}}{c}\cdot\Delta\cdot(n-1)\cdot sin(\phi)} \end{bmatrix} \tag{2.7}$$

[2]The presented operation works only on a communication system where the number of transmit antennas is equal to the number of receive antennas. When this is not the case this synchronization functionality has to be modified. However as the synchronization is not the main topic of this research and the presented solution suffices, this will therefore not be further addressed.

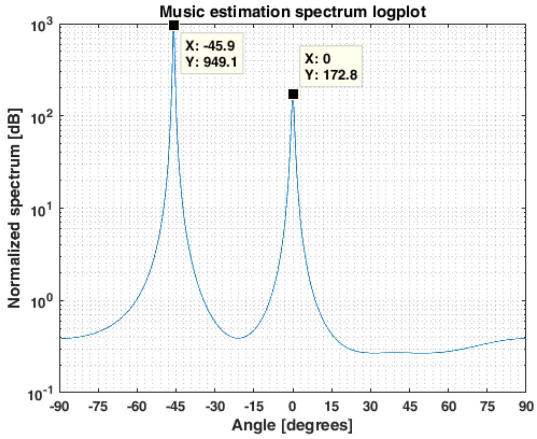

Figure 2.6: Direction of Arrival results by employing the MUSIC algorithm.

The noise subspace, **En**, will be spanned by selecting the eigenvectors that correspond to the lowest n eigenvalues (in which n depends on the desired dimension of the signal subspace). The product of the steering vector with the noise subspace should be high everywhere except for the angles in which a signal resides. By finding the peaks resulting from equation 2.8, the DOA's can be obtained.

$$\mathbf{P} = \frac{1}{\mathbf{a}(\phi) \cdot \mathbf{En} \cdot \mathbf{En}^* \cdot \mathbf{a}(\phi)} \tag{2.8}$$

Figure 2.6 shows the results of MUSIC graphically for a system with two incoming wavefronts, one from 0° and one from -45°(which is the situation of figure 2.4). This plot has been made by selecting two eigenvectors for the noise subspace and that the MUSIC algorithm indeed produces peaks at 0°and -45°.

2.7 Interference suppression and reduction

In section 2.4.3 it was explained that spatial multiplexing operates by applying a singular value decomposition on the channel matrix to determine a set of singular vectors. These vectors are created by an estimation of the channel matrix. When estimating the channel matrix, interference may be present in the system. The interference introduces significant errors as the estimation of the channel will find a correlation between received signals and transmitted pilot signals which are caused by the interference and not by the actual transfer between transmitter and receiver. The channel estimation itself may also become impossible when the system cannot distinguish the training sequence because of the interference.

The concepts of the MUSIC algorithm from section 2.6 can be used to remedy this phenomenon. When the receiver array is used to make a direction of arrival analysis while the transmitter of its own communication system is silent, a profile can be made for the interference in its surroundings. This interference profile is composed of a set eigenvectors **V** and the corresponding eigenvalues **D**. When a single interferer is present the DOA algorithm would give a peak from a certain angle, which would, according to section 2.6, belong to the signal subspace. The three other vectors (in case of an array consisting of four antennas) would then be orthogonal to this subspace and should therefore be clear of any interference. If the vector related to the interferer is removed from the set of eigenvectors **V**, a 4x3 matrix **F** is created. This matrix can be used as a transformation matrix on the received samples ($\mathbf{Y}$) to create $\mathbf{Y_{filtered}}$ (See equation 2.9). In this operation the matrix $\mathbf{F}^*$ will act as a spatial filter, because the subspace that holds the interference was removed from this matrix[3].

$$\mathbf{Y_{filtered}} = \mathbf{F}^*\mathbf{Y} \tag{2.9}$$

Because $\mathbf{F}^*$ is a 3x4 matrix, the dimension of $\mathbf{Y_{filtered}}$ will be reduced by one. This results in the channel estimation producing a 3x4 matrix as the system now transmits four channels and the estimation is performed by only three receiver signals. The eigenvectors that are used in $\mathbf{F}^*$ also contain phase rotations, which cause the received signals $\mathbf{Y_{filtered}}$ to be in a different coordinate frame. The left singular vectors of the singular value decomposition now no longer only relate to the phase shifts required for the steering vectors, but also the ones for the filter. This can be resolved by left-multiplying $\mathbf{Y_{filtered}}$ with $\mathbf{F}$, which results in the operation as shown in 2.10.

$$\mathbf{Y_{filtered}} = \mathbf{F}\mathbf{F}^*\mathbf{Y} \tag{2.10}$$

Since the eigenvectors of $\mathbf{V}$ are orthonormal, the column vectors of $\mathbf{F}$ are also orthonormal. $\mathbf{F}$ is thus an n by n-1 matrix with orthonormal columns. For such matrices holds that $\mathbf{F}\mathbf{F}^*\mathbf{Y} = proj_W\mathbf{Y}$ for all $\mathbf{Y}$ in $\mathbb{C}^n$, where W is the column space of the matrix $\mathbf{F}$[15, p42]. This proves that equation 2.10 effectively projects the signals of $\mathbf{Y}$ onto a n-1 dimensional space (which does not contain the subspace that belongs to the interference) and back to the original coordinate frame that once again holds n dimensions.

This approach does have a downside. The modified transformation matrix was determined solely on the presence of interfering signals (the system's own transmitters were mute). This means that the subspace vectors that are conserved are completely unrelated to the channel between transmitter and receiver. It may thus very well be possible that there are nulls present for angles that are in fact necessary for spatial multiplexing in that situation. The impact of this shortcoming reduces as the number of antennas in the array increases. The remaining subspace vectors are based on White Gaussian Noise (WGN) and should thus spread themselves out over the angular spectrum, whilst all having a null at the angle of the interferer. With more antennas in the array, there are more degrees of freedom available for the null steering giving a more balanced result.

The spatial multiplexing algorithms will now use $\mathbf{Y_{filtered}}$ instead of $\mathbf{Y}$. Every signal coming from the angle of the interferer will be suppressed by the spatial filter. The left singular vectors will thus be impervious to signals from this angle and their angular sensitivity plots should therefore show a null at this angle.

In this research the data flows solely from transmitter to receiver, in other words, the arrays do not switch roles. In a normal communication system the data is usually bi-directional. In these cases the acquired interference profile could also be used to avoid allocating power to steering vectors which are pointing towards the source of the interferer, effectively reducing the interference footprint of the system.

[3]A similar approach has been used in [14].

Chapter 3

Simulations

In this section the practical feasibility of the deposed theories will be shown. This will be done by a Matlab simulation of a case which is the mirrored counterpart of figure 2.4. So in this case the reflective surface is 'above' the arrays instead of 'below'. The first step is to create a virtual representation of this situation. In order to do this, two antenna arrays are instantiated six meters apart. Figure 3.1 shows how this use case is modeled in Matlab. In this figure, the two antenna arrays are shown, the transmitting array is in blue on the left, the receiving antenna array is depicted in red on the right. The light blue line indicates a reflection surface and is used to determine the path length and phase shift of the reflective path.

Assuming the virtual wall is a perfectly reflecting surface (all incoming power is reflected), the received signals can be modeled by mirroring the reception array with respect to the reflecting surfaces. The received signals can thus be modeled as a superposition of the signals received by the direct path (red array) and the signals received by the reflection (yellow array).

An artificial channel matrix is created by calculating the distance between each of the antenna pairs (both blue - red as blue-yellow). Based on these lengths phase shifts are calculated. Using these distances and Friis formula for free path loss[16], the path loss is calculated. When

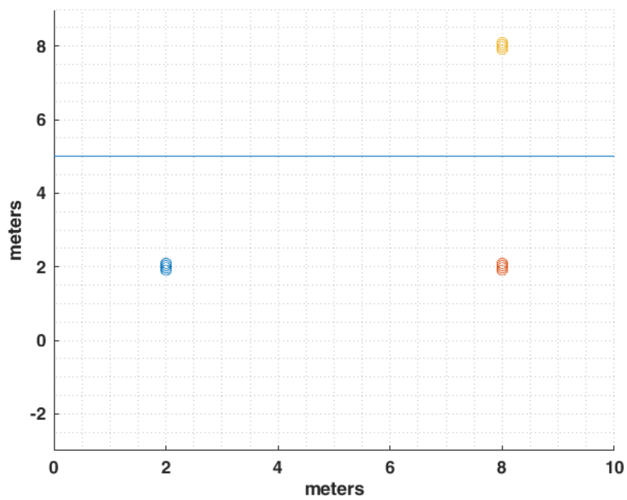

Figure 3.1: System model in Matlab with the receiving array in red and the transmission array in blue.

the gain and phase changes are combined, these create the complex channel matrices for both the direct path and the reflective path. By means of superposition, these channel matrices can then be summed to give the resulting channel matrix.

3.1 Estimation of the channel

A virtual environment has been instantiated in which two paths are possible, a direct path and a reflection. These give rise to an artificial **H** matrix. In this section the actual estimation of the channel will be performed and the goal will be to have an accurate estimate of the channel matrix **H**.

First a scenario without any noise is investigated. Figure 3.2 shows the (real part of) the training signal. It is chosen to be a single period of a sine wave. which is active on only one of the four transmitter channels at a time. By applying equation (2.2), the sampled signals at the receiver can be determined. The resulting signals are shown in figure 3.3.

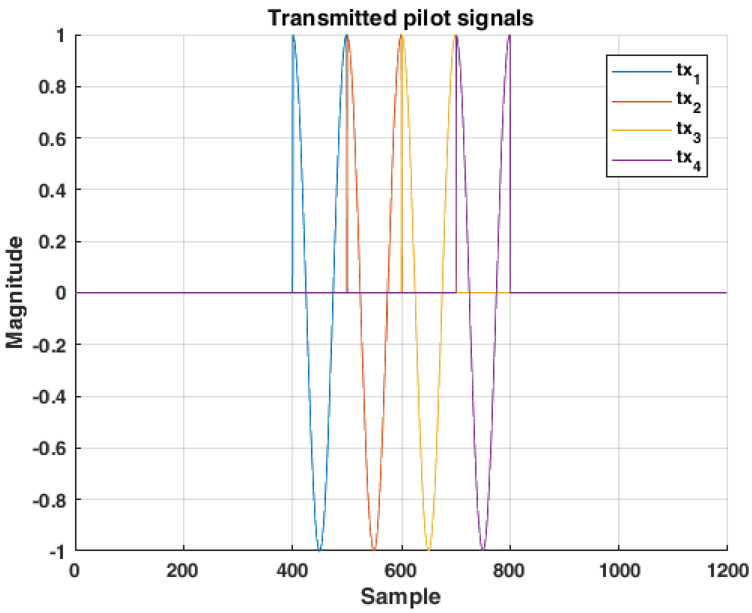

Figure 3.2: The in-phase components of the pilot signal to be used for the estimation of the channel matrix.

Using the least squares estimator of equation 2.3, an estimation can be made of the channel matrix ($\mathbf{H_{est}}$) for a situation without noise. Table 3.1 shows the estimated channel matrix in polar form for the situation presented in figure 3.1 and table 3.2 shows the actual **H** matrix ($\mathbf{H_{act}}$) for this case.

Table 3.1: Estimation of the channel matrix

3.61e-03 ∠ -22°	3.27e-03 ∠ 30°	8.58e-04 ∠ -27°	3.73e-03 ∠ -9°
3.27e-03 ∠ 30°	9.42e-04 ∠ -35°	3.82e-03 ∠ -13°	2.86e-03 ∠ 39°
8.58e-04 ∠ -27°	3.82e-03 ∠ -13°	2.77e-03 ∠ 36°	1.54e-03 ∠ -43°
3.73e-03 ∠ -9°	2.86e-03 ∠ 39°	1.54e-03 ∠ -43°	3.96e-03 ∠ -4°

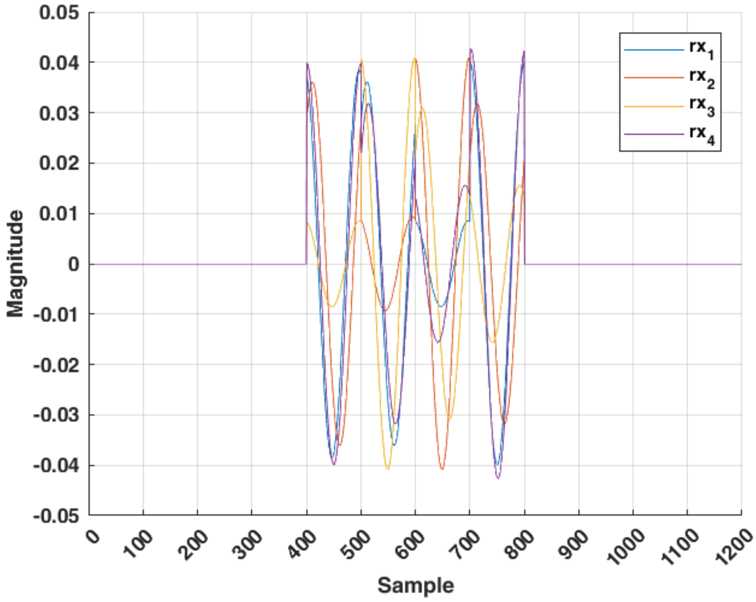

Figure 3.3: The in-phase response of the pilot signal on the receiver array.

Table 3.2: Actual channel matrix

3.61e-03 ∠ -22°	3.27e-03 ∠ 30°	8.58e-04 ∠ -27°	3.73e-03 ∠ -9°
3.27e-03 ∠ 30°	9.42e-04 ∠ -35°	3.82e-03 ∠ -13°	2.86e-03 ∠ 39°
8.58e-04 ∠ -27°	3.82e-03 ∠ -13°	2.77e-03 ∠ 36°	1.54e-03 ∠ -43°
3.73e-03 ∠ -9°	2.86e-03 ∠ 39°	1.54e-03 ∠ -43°	3.96e-03 ∠ -4°

To compare the estimation with the actual channel matrix, equation 3.1 gives a definition of the estimation error.

$$\mathbf{H}_{\mathbf{est\_err}} = \left\| \frac{\mathbf{H}_{\mathbf{act}} - \mathbf{H}_{\mathbf{est}}}{\|\mathbf{H}_{\mathbf{act}}\|} \right\| \tag{3.1}$$

Applying this to the found values of tables 3.1 and 3.2 gives:

Table 3.3: Error of the estimation of the channel matrix without noise.

1.6968e-16	4.4418e-16	6.3188e-17	2.3408e-16
1.8728e-16	1.1508e-16	1.1356e-16	3.0295e-16
6.3188e-17	0	7.8170e-17	1.9858e-16
2.9034e-17	3.3871e-16	1.4042e-16	1.3691e-17

As the estimation error is approaching zero it can be said that the estimation predicts **H** almost perfectly. This is not surprising as only rounding errors could affect this estimation.

If WGN is added to the received signals of **Y**, the estimate become less accurate. Table 3.4 shows the estimation error for a scenario when the SNR is 10dB.

Table 3.4: Error of the estimation of the channel matrix with noise present (SNR = 10dB).

4.0017e-02	4.3926e-02	6.6975e-02	4.4794e-02
4.3367e-02	6.7147e-02	2.4377e-02	9.6916e-02
1.7447e-01	6.3770e-02	6.2151e-02	1.0674e-01
2.3336e-02	3.4314e-02	1.7241e-01	5.2352e-02

As the noise is usually random in nature, its effects can be negated by averaging over multiple instances. This can be achieved by extending the pilot signal. Table 3.5 shows the results with the pilot signal repeated 100 times. It effectively reduces the standard deviation of the noise by a factor $\sqrt{q}$, where q is the number of repetitions. For the given matrices, it can be calculated that the error between the elements of these matrices has been reduced by a factor 12.3 on average[1]. This technique thus introduces a trade-off between the accuracy of the estimation and the cost of a longer training sequence.

Table 3.5: Error of the estimation of the CSI with noise present (SNR = 10dB) and with extended training signal (100 repetitions) .

3.5514e-04	1.7690e-03	9.5719e-03	3.1396e-03
1.5426e-03	1.0356e-02	4.2938e-03	1.6124e-03
1.8506e-02	1.5177e-03	6.0960e-03	9.4218e-03
3.7378e-03	3.6580e-03	9.1505e-03	1.2683e-03

3.2 Decomposing the channel matrix

In the simulation example two paths are present: a direct path and a reflection. WGN noise is added to achieve an SNR of 10dB. Table 3.6 shows the resulting singular values when an SVD is performed on the channel matrix. The ratios between the singular values are given in table 3.7.

Table 3.6: Singular values for the estimated channel matrix of the simulations.

0.0104	0	0	0
0	0.0055	0	0
0	0	0.0003	0
0	0	0	0.0000

Table 3.7: Condition ratios for the estimated channel matrix of the simulations.

1.0000	1.8693	30.2804	308.9373

For two eigenmodes, the ratio between the first and second singular value is still close to one. When three eigenmodes are selected, the ratio increases significantly (up to 30.3) which is undesirable. The theorem indicates thus that there are two dominant orthogonal paths present in the system.

It should be noted that the singular values are dependent on the physical setup. It is here where the angular separation comes into play. When looking at the angular sensitivity plot

[1]This factor will approach 10 if the estimations of the errors are repeated enough times.

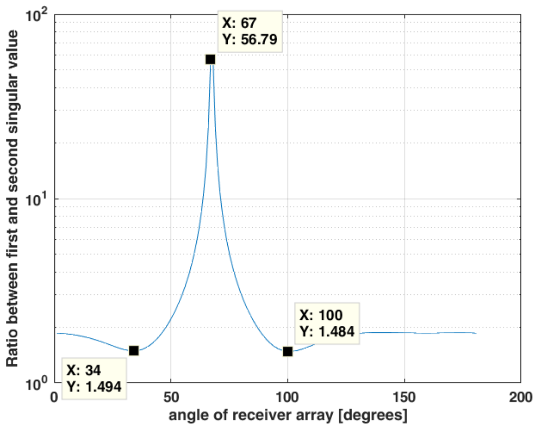

Figure 3.4: Ratio between the first and second singular value plotted against the angle of the receiver array..

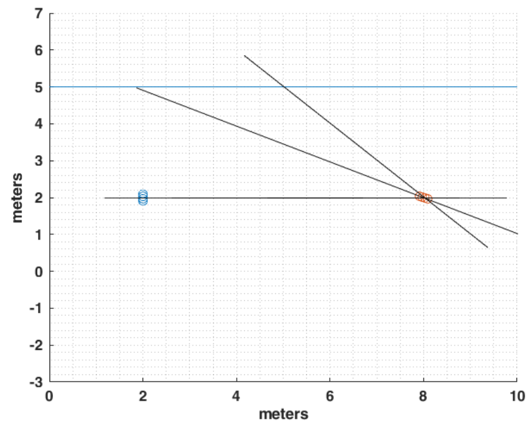

Figure 3.5: Angles of incidence visualized for the worst case scenario.

of figure 2.2, it is easily understood that any system works best if the steering angle for an eigenmode has a strong gain in the direction of that eigenmode, while at the same time having a strong rejection towards the directions of other eigenmodes. It is for this case that the eigenmodes are as orthogonal as possible and thus give rise to a low condition ratio between the first and second singular value. To illustrate this further, the receiver antenna array is rotated around its center, which results in different angles of incidence for the direct path and the reflection, whilst keeping the angular separation constant. Figure 3.4 shows the ratio between the first and second singular value for a system with two eigenmodes against the rotation of the receiver array.

A rotation of 67° results in the worst case scenario. For this angle the second singular value is smallest compared to the first singular value. When this case is visualized (see figure 3.5) it becomes clear as to why this is: the angle of the impinging signals, relative to the angle of the array in space, is identical. Due to the nature of the linear phased-array antenna, it cannot distinguish between signals coming from for instance 75°and 105°. For both of these angles, the delay profile of the signals on each antenna is the same with respect to its mirrored counterpart resulting in no angular separation whatsoever [2].

[2]This could be solved by not using a linear antenna array but a matrix configuration instead.

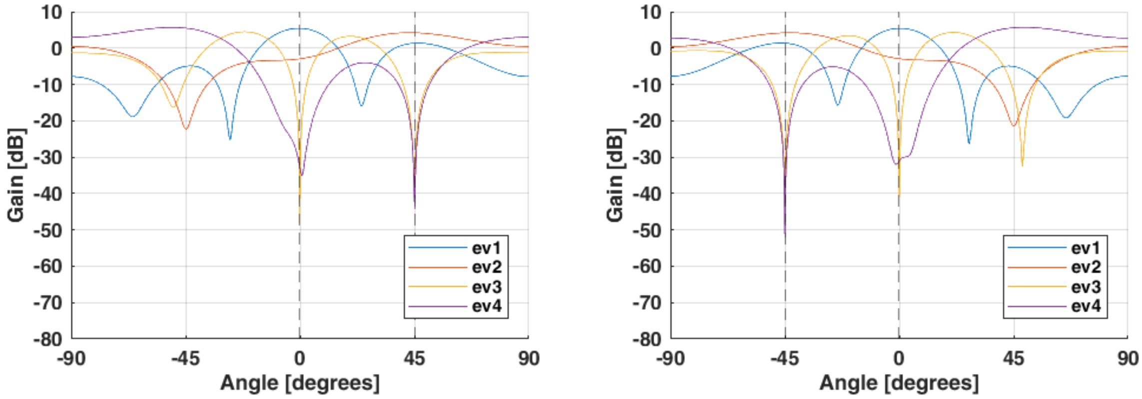

(a) Left singular vectors, **U**.

(b) Right singular vectors, **V***.

Figure 3.6: Directional sensitivity of the singular vectors for the simulations. The dashed lines indicate the direct path (0°) and the reflective path (respectively 45° and -45° for **U** and **V***)

Section 2.4.3 also addressed the use of the $\mathbf{U}$ and $\mathbf{V}^*$ matrices. The vectors from these matrices can be used as a coordinate transforms on respectively the receiver and the transmitter side. This implies that the vectors of these matrices could be interpreted as steering vectors for the array. Using the simulation results this can be visualized. Figure 3.6 shows the directional gain when these vectors are treated as steering vectors for the array.

In the simulation the receiver was subjected to signals originating from 0° (the direct path) as well as signals from 45° (the reflection). Figure 3.6a shows the visualization of the left singular vectors. In this figure, *ev1* is the left singular vector corresponding to the first singular value, *ev2* to the second singular value, etc. It is shown that the first left singular vector has a strong gain in the direction of 0° and that the second left singular vector shows a strong gain in the direction of 45°. These coincide with the angles from which the signals arrive.

The right singular vectors of figure 3.6b can be addressed in the same way. These should represent the angles at which the transmitter is focusing its wavefronts. In this figure it is shown that the first singular vector is directing its efforts at 0°, which coincides with the direct path. The second singular vector is pointing towards -45° which is the direction of the reflective surface.

The last two singular vectors of both the $\mathbf{U}$ and $\mathbf{V}^*$ matrices are not as important. Their singular values show that these eigenmodes are much weaker than the first two and are therefore unlikely to be used. When analyzing their angular behavior it can be seen that these are mostly shaped in such a way that they have a high rejection for angles for which the first or second singular vectors have peaks.

The singular value decomposition will always result in a number of eigenmodes equal to the minimum number of antennas in one of the arrays ($n_{eigenmodes} = min(n_t, n_r)$. In a rich scattering environment, the amount of spatial paths from transmitter to receiver may be larger than the number of eigenmodes of the system. The eigenmodes will then be determined by a combination of multiple spatial paths. This means that in such an environment, the maximum gain of the singular values can no longer be used solely for determining the spatial paths, as the power transmitted to other angles might contribute to the eigenmode as well.

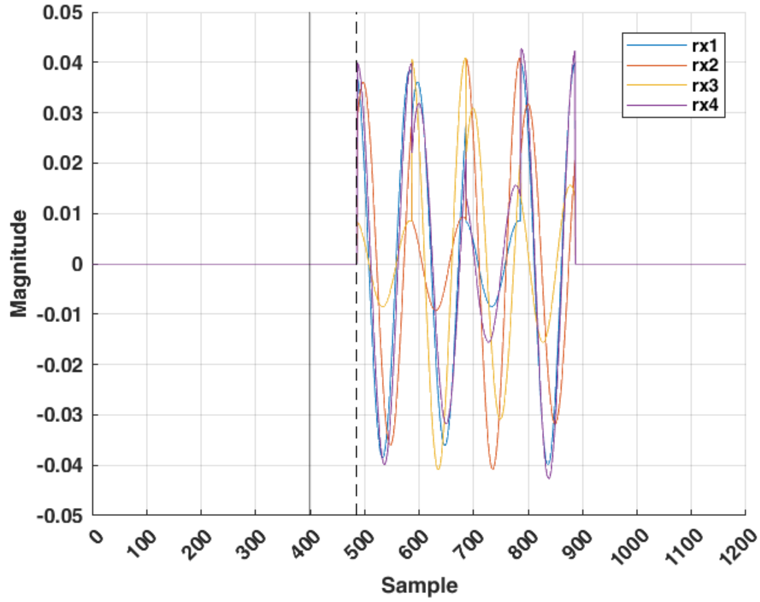

Figure 3.7: The response of the pilot signal on the receiver array with an arbitrary shift in samples present. The dashed line with respect to the solid black line indicates the shift in samples.

3.3 Synchronization

When the received signals have an offset in samples compared with the training signals, synchronization of the signals is required. Figure 3.7 displays such an offset. It is the same response as figure 3.3, but here the samples of the receiver are shifted by 85 samples. The correlation between the received signals and the training signals can be found by performing a cross correlation.

After summing the cross correlation of the channels for every sample, the plot of figure 3.8 can be found. This plot shows the combined correlation against the number of samples shifted. The maximum combined correlation is at sample 85. This shift can then be used to synchronize the signals. The described approach is quite rudimentary and more advanced synchronization techniques exist. However, the proposed approach is sufficient for this research and because synchronization is not one key topics of this research, it will not be further addressed.

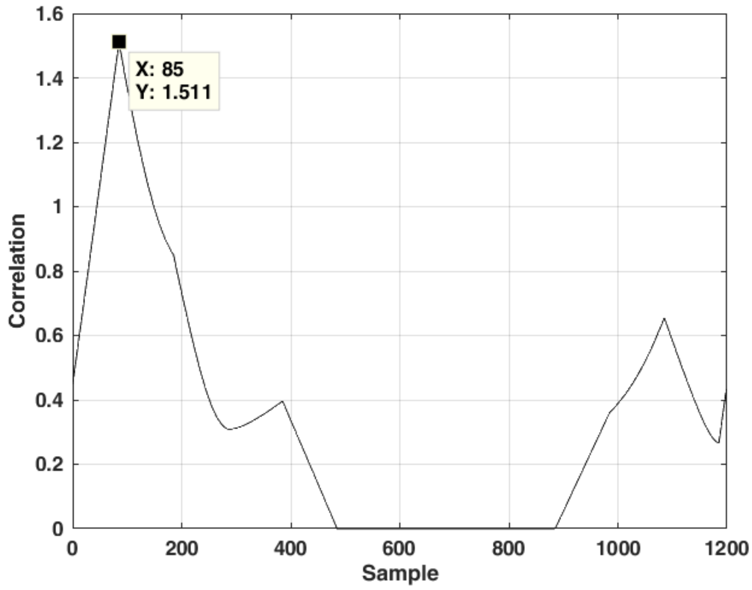

Figure 3.8: Results of the correlation between the pilot signal and the response on the receiver.

Chapter 4

Setup

One of the goals of this project is to verify the theory with actual experiments.This section will present the setup that is used to perform the experiments for this project.

4.1 System platform

The setup is based on the *Analog Devices FMCOMMS5-EBZ*. This device is a breakout board which will extend a *Xilinx ZC706 SoC*. The FMCOMMS5 is an evaluation board that houses two AD9361 chips. Both of these chips contain two fully functional transceiver chains. The FMCOMMS5 board itself contains logic to synchronously deploy these transceiver chains, making a 4x4 transceiver system possible. The FMCOMMS5 board is an evaluation board produced by Analog Devices to show the capabilities of the AD9361 chips and also how they can be employed in unison. Even though this board only houses two chips, it is meant to show the ability to extend the amount of transceiver chips on the PCB to create even larger arrays.

There are two ways of operating the hardware. The first is by using a provided Linux design. This Linux design loads a lightweight Linux distribution onto the SoC. The Operating System (OS) utilizes the ARM core inside the ZC706. The AD9361 chips are controlled by IP cores loaded onto the FPGA fabric (illustrated in figure 4.1 by the blue box named 'AD9361 core'). The ARM uses the AXI and AXI Lite busses to communicate with the FPGA fabric. The AXI Lite bus is also used for SPI communication with the FMCOMMS5 board itself. Figure 4.1 shows a block diagram of this system. On the left the Xilinx ZC706 SoC is shown and on the right the Analog Devices FMCOMMS5-EBZ transceiver breakout board is shown.

It is also possible to use the hardware without an operating system and control all the hardware using the no-OS drivers [17]. A custom application can then be created using the Xilinx SDK software which interfaces with the hardware using the provided API. This creates the opportunity for a lightweight implementation with only the bare minimum functionality and a custom interface. The Linux distribution, however, offers all the controls that are required so the no-OS option will not be used.

4.1.1 AD9361

Receiver chain Each of the two AD9361 chips contains two complete transceiver chains. A block diagram of both the transmitter and the receiver can be seen in figure 4.2. Each receive chain has three inputs: RxA, RxB, RxC. RxA is a wide band receive chain for a bandwidth of 70MHz up to 6GHz, RxB is a narrow band receive chain specially designed for 2.4-2.5GHz. RxC

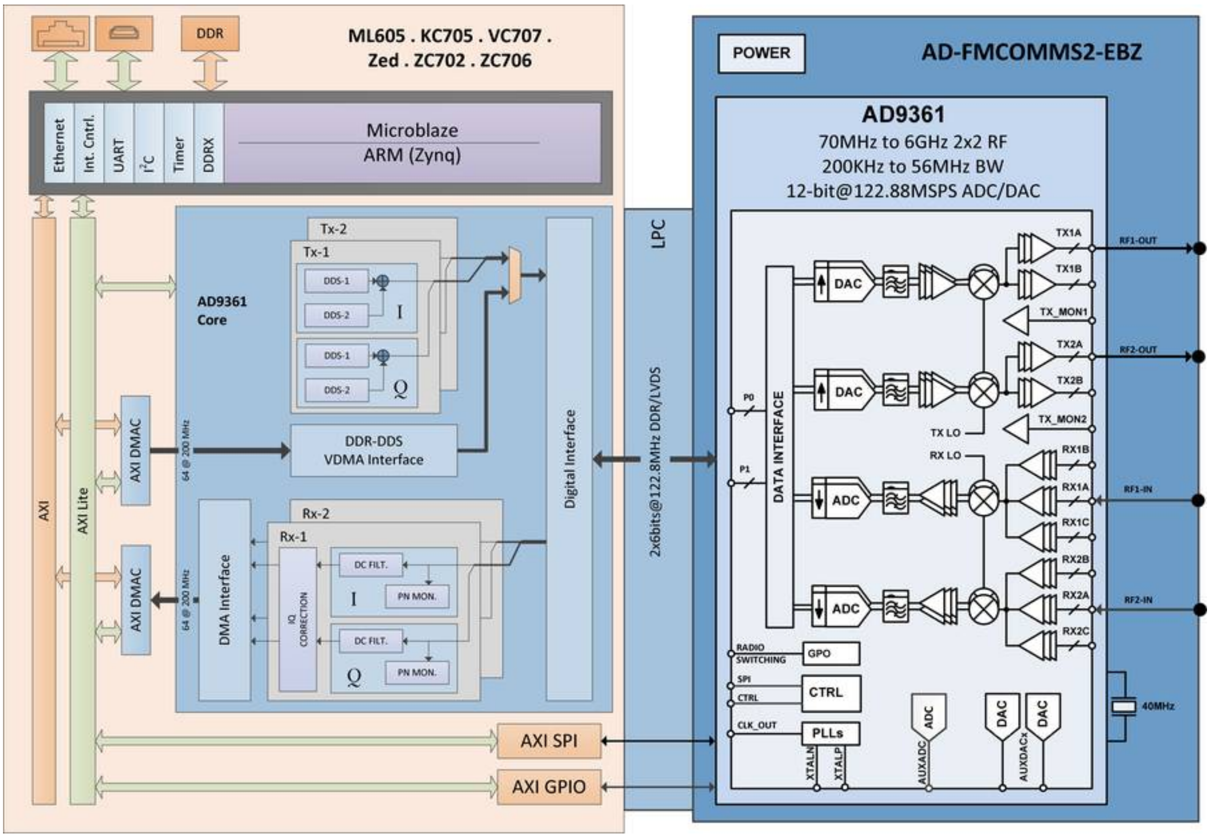

Figure 4.1: Block diagram of the Xilinx Zynq ZC706 SoC and the Analog Devices FMCOMMS5-EBZ transceiver board.

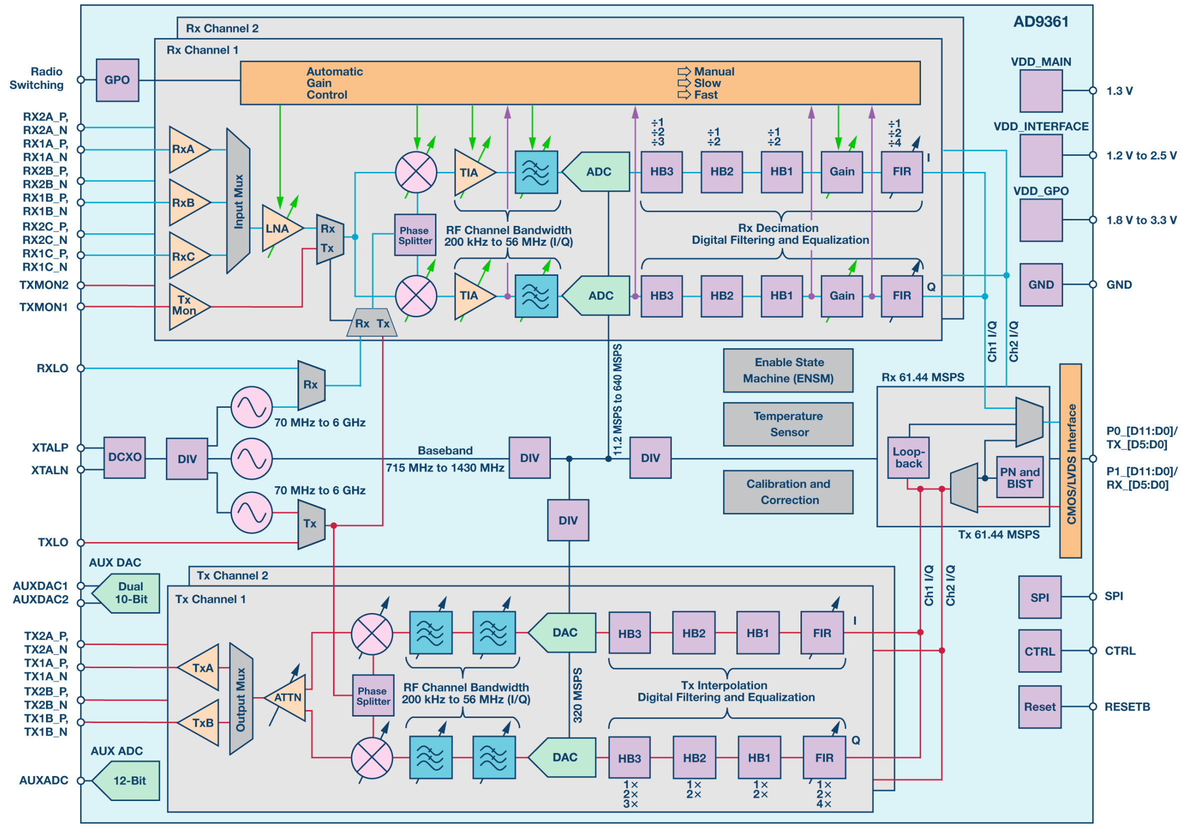

Figure 4.2: Block diagram of the AD9361 transceiver chip.

has no outside connections but is instead used for internal loopback purposes. The receive chain further incorporates an LNA with variable gain, an IQ demodulator, a 12bit 640MSPS sigma delta converter and wide variety of digital filters for decimation and equalization purposes. All experiments done in this projects are performed using the wide band receive chain of RxA.

The gain path is controlled by the software itself. Using the Graphic User Interface (GUI) the desired gain of the total receiver chain can be set for a range of 0dB up to 73dB. The software decides how this gain can be distributed best among the LNA, the demodulator, the Transimpedance Amplifier (TIA) and the filters.

Transmitter chain The transmission chain is also shown in figure 4.2. This chain features some filters for interpolation and equalization as well as controlling the channels bandwidth. It features a 12bit DAC and a quadrature modulator block. The transmitters have a maximum output power of 7.5dBm which can be attenuated over a 90dB range in steps of 0.25dB. For further specifications refer to the datasheet of the AD9361[18].

4.1.2 Software

The hardware platform will be employed using the provided Linux design. When the device is powered on, the OS is loaded from the SD-card automatically. The OS initiates the Linux LibIIO subsystem which handles the interfacing of the OS with the hardware. Using these libraries, device settings can be altered by changing a parameter in a text file. The Linux design also features an application called ADI IIO Oscilloscope (See appendix A). This application uses the underlying LibIIO library to create a GUI where most of the device settings can be adjusted

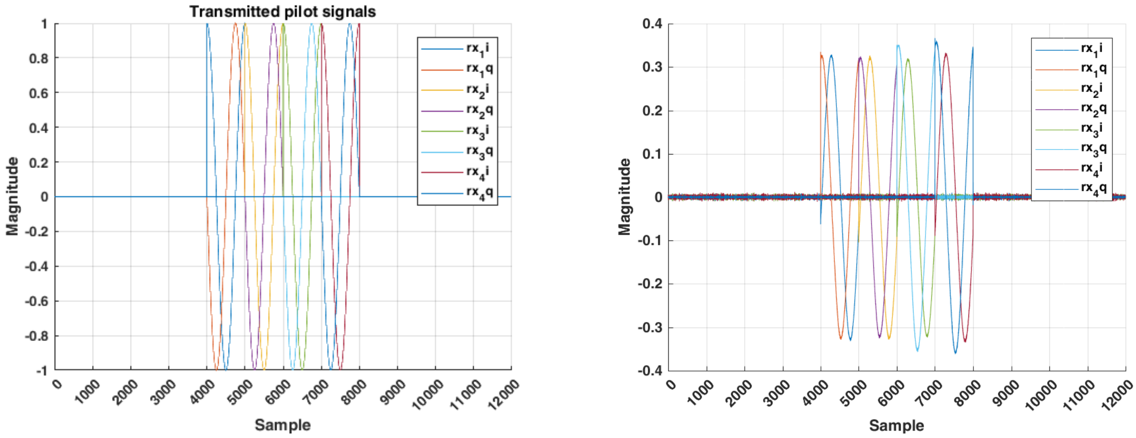

(a) DAC output buffer pilot signals. (b) Acquired ADC samples.

Figure 4.3: Example measurement using loopback cables between each respective transmitter receiver pair.

(see appendix B). It also features an oscilloscope function where signals can be loaded into the DAC buffers after which both the transmitter and the receiver can be initiated. The device then uses the data in the DAC buffers to transmit signals using the transmit chain. Simultaneously, the receive chain will start sampling data from the receiver antennas. This feature will be used for most of the project. The application is able to process signals in its buffer of up to 2^{20} samples with each of these samples consisting of 12 bits. The ADC buffers can be read out and saved to comma separated file (csv) files, as well as to Matlab files.

4.1.3 Measurement procedure

Signals are transmitted by the transmitter chains of the hardware for the experiments. The signals are stored into plain text files which can be processed by the software. Using the ADI IIO Oscilloscope, these are loaded into the DDR-DDS VDMA interface of the FPGA (see figure 4.1). After setting the transmitter attenuation, the receiver gains, the bandwidths and the LO frequencies, a single shot capture is performed. The ADC's and DACs are enabled synchronously to initiate a transmission. Figure 4.3b shows an example of such a measurement with cables connected from the SubMiniature version A (SMA) connectors of the transmitters straight back to the SMA connectors of the receivers. To obtain these results, the pilot signal of figure 4.3a is used.

Of each of the four channels both the in-phase and the quadrature response is captured and plotted. On the x-axis the samples numbers are shown and on the y-axis the values produced by the ADCs. The ADC's map the input voltage onto 12 bit values with a full scale voltage of 0.625V (0dBFS) . In most figures of measurements, the y-axis will have a unit displayed simply as 'magnitude'. The values shown should be interpreted as a factor of this full scale value. A value of 0.3 is equivalent with 0.3*0.625V=0.1875V measured at the ADC.

As the pilot signals used are a full period of a sine wave, it does not really add value to plot both the in-phase and the quadrature component of each channel[1]. Some plots will therefore omit the quadrature components and just show the in-phase components. When this is the case

[1]If only a fraction of a complete period was shown, you would need the quadrature component to determine the magnitude of the signal.

the legend will just list rx_1 ... rx_4.

4.1.4 Analog setup

For the analog part of the system two linear phased array antennas are used, both consist of four antennas spaced 6.25cm apart (half a wavelength of 2.4GHz). The antennas[19] are mounted on a platform made from PVC material and are connected to the FMCOMMS5 board by means of six meter SMA cables.

Experiments will be performed in two situations. The first is carried out inside an anechoic chamber, which serves as a controlled environment. The second type of experiments will be held in a normal lab room, which is not equipped with any kind of adsorbing material. The distance between the arrays will be made identical to the distance in the anechoic chamber for optimal comparisons.

4.1.5 Power calculations

To determine the required configurations for the transmit and receive chains, a rough estimate of the power levels has to be made. Losses originate in several forms: the Free Space Path Loss (FSPL), reflections at interconnecting ports and cable losses.

Free Space Path Loss The FSPL can be determined by using Friis formula[16], which is shown in equation 4.1.

$$P_R = P_T G_T G_R (\frac{\lambda}{4\pi d})^2 \tag{4.1}$$

This equation relates the transmitted power to the received power on a linear scale. As power calculations are usually performed on a logarithmic scale, equation 4.2 shows the same relation for a logarithmic scale. Here P_T and P_R are the transmitted and received power levels in dBm. G_T and G_R are the effective isotropic gains in dBi of the receiver and transmitter antennas.

$$P_R = P_T + G_T + G_R + 10log_{10}((\frac{\lambda}{4\pi d})^2) \tag{4.2}$$

For the experiments a distance of 2.9 meters between the antenna arrays will be used. The antennas used have an effective isotropic gain of 1.5dB. The transfer $P_R - P_T$ can then calculated to be -46.3dB (equation 4.3).

$$P_R - P_T = 1.5 + 1.5 + 10log_{10}((\frac{0.125}{4\pi \cdot 2.9})^2) = -46.3dB \tag{4.3}$$

Reflections As with any 2 port, the connections between the antennas and the transceiver board are subject to scattering parameters (S_{11} and S_{22}). The transceiver board, as well as the antennas, have a reflection coefficient of max -10dB. Assuming the worst case scenario, at each of these interconnections 10% of the power is reflected. For four interfaces in each path, the maximum expected loss from these reflection is thus: $10log_{10}(0.9^4) = 1.8dB$.

Cable Loss To connect the antennas to the transceiver board, SMA cables will be used. These cables have a measured loss of about 1.2dB/m at 2.4GHz. For a total cable length of twelve meters (six meters for both the receiver antennas and the transmitter antennas), a loss can be expected of 14.4dB.

Input Power The ADC has an input swing of -625mV to 625mV. Using this characteristic the maximum input power can be calculated when taking into the account that the channel is 50Ω. Equation 4.4 shows that the maximum input power at the receiver is 5.9dBm.

$$P_{max} = 10 * log_{10}(V_{RMS}^2/R) = 10 * log_{10}((\frac{0.625}{sqrt(2)})^2/50) + 30 = 5.9dBm \tag{4.4}$$

4.1.6 Power verification

To check these figures for the actual setup, the power levels of figure 4.3b will be analyzed. In case of figure 4.3b the ADC output is about 0.33 full scale. This is equivalent to a measured voltage of $0.33 \cdot 0.625 = 0.21V$ or $0.15V_{RMS}$. All interfaces are 50Ω terminated giving a total input power of $\frac{0.15^2}{50} = 4.3 * 10^{-4}W$ or -3.7dBm. For this measurement the receiver gain was set to 0dB and the transmitter power was set to -2.5dBm. This results in a 1.2dB loss of signal. A 30cm cable would account for roughly 0.4dB while the two interface connections would account for 0.9dB resulting in a 1.3dB loss of signal, which is a sensible result.

4.1.7 Configuration

As it is unnecessary to use the maximum transmission power over small distances, the transmitters are attenuated by 10dB to a power level of -2.5dBm. Equation 4.5 shows the expected loss in dB of the entire path from transmitter to receiver to be 62.5dB. The receiver gain is therefore set to 60dB. The transmitted power will be set to -2.5dBm. Unless otherwise specified, the experiments are performed at 2.45GHz using a bandwidth of 18MHz and a sampling rate of 30.72Mega Samples Per Second (MSPS).

$$G_{path} = G_{Pathloss} + G_{Cableloss} + G_{S11} = -46.3 - 14.4 - 1.8 = -62.5dB \tag{4.5}$$

4.2 Anechoic chamber

Some of the exeriments are carried out inside an anechoic chamber (See appendix C). Such a room is a faraday cage that is padded on the inside with EM absorbing cones. The room that was used in these experiments was made by Comtest[20]. It's dimensions are roughly four by four by three meters (l,w,h) and the room is filled with cones of the type MT45 flat tip [21]. Figure 4.4 shows the return loss of these cones in ideal conditions. The cones provide a return loss of 45dB up to 50dB for frequencies of 1.4GHz and 2.4GHz respectively.

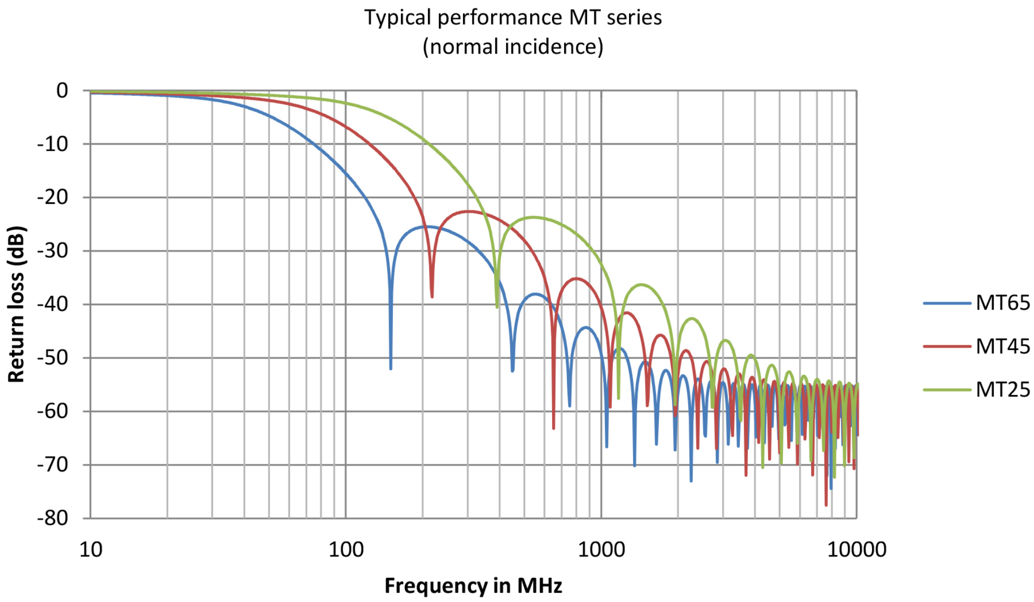

Figure 4.4: Return loss for the MT45 cones present in the anechoic chamber.

Chapter 5

Experiments

Various experiments will be performed to address the theories explained earlier. In section 4.1.7 settings for the receiver gain and the transmit power were mentioned to be $G_{rx} = 60dB$ and $P_{tx} = -2.5dBm$. If not explicitly mentioned otherwise, these are used in all the experiments. In total four sets of experiments are presented:

- Anechoic Chamber
- Coupling
- External Amplification
- Practical Environment

5.1 Anechoic chamber

The first experiment is performed inside an anechoic chamber. The goal of this experiment is to confirm the theories presented in chapter 2 by relating the simulations of chapter 3 to the processed results of the experiments.

5.1.1 Method

The use of an anechoic chamber is required to have as much of a controlled environment as possible. The simulations of chapter 3 assumed that there were no signal sources other than the systems transmitter array and also that there only exists a direct path and a single reflection path at an angle of 45°with respect to both the transmitter as receiver array. In an anechoic room there should be only a direct path present. A secondary path can be created by adding a reflective surface inside the chamber.

The complete system is placed inside the anechoic chamber as depicted in figure 5.1. This implies that the cables can be of short length, but also that both the ZC706 as the FMCOMMS5 board are inside the room. Theoretically the clock lines or the fan that cools the FPGA and ARM could influence the measurements. The only line going out of the anechoic room is an ethernet cable by which the system is controlled remotely. This has the benefit that all cables for the measurements remain inside the anechoic chamber.

Both the receiver array and the transmitter array are placed inside the room without any reflective surface. The recceiver array is connected to the transceiver board using 1m SMA cables, whilst the transmitter is connected by an extended SMA cable with a length of 6m. The

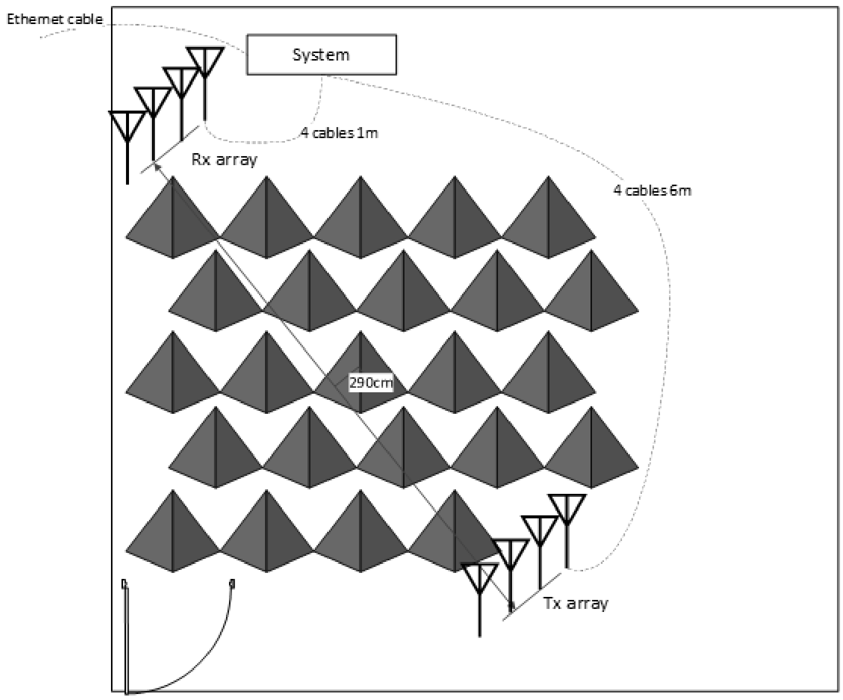

Figure 5.1: Setup for the first experiment in the anechoic chamber.

pilot tone of figure 5.3 is used, which is composed of four single periods of a sine wave that are active on each of the different transmitter antennas at different times.

The provided IIO Scope application is used to both transmit and receive the samples. The received signals are saved and loaded into Matlab for further analysis. A time shift is performed on the received samples to synchronize the received signals with the pilot signals. An estimation of the channel matrix is made and a singular value decomposition is performed on the channel matrix. The resulting singular values and singular vectors are then evaluated to determine whether the results are according to expectations.

In the situation of figure 5.1 only a direct path is present (in an anechoic chamber all the reflections are absorbed), therefore it is expected that the first singular value is significantly larger than the others. The antenna arrays are positioned on both sides of the chamber in such a way that they are directed at one another (see figure 5.2). It is expected that the left singular vector corresponding to the largest singular value shows a strong sensitivity to an angle of 0°.

When a reflective surface is added, a second strong singular value is expected to appear. This second singular value is accompanied by another left singular vector which should be sensitive towards the reflective surface instead of toward the transmitter array.

For the experiments in this section the output power of the transmitter is set to -2.5dBm. The receiver chain is set to a total gain of 60dB. The distance between the two antenna arrays is 2.9m.

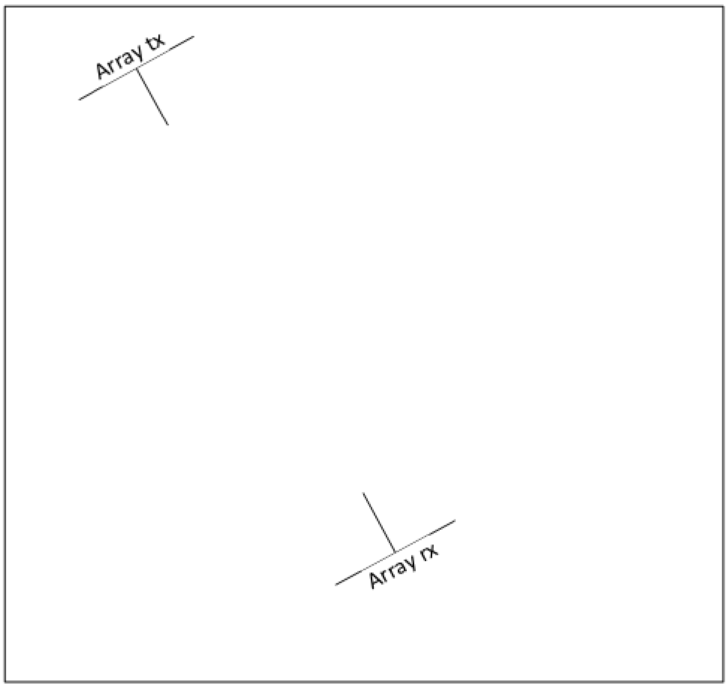

Figure 5.2: Orientation of the antenna arrays.

5.1.2 Results

Figures 5.3 and 5.4 show both the transmitted pilot signal and the captured response of the receiver array. The way in which the amplitudes vary between the various receiver antennas is remarkable. Some variation in amplitude can be explained by constructive and destructive interference, due to coupling between the antennas and due to shadowing effects, but the amount of variation shown in figure 5.4 exceeds realistic values for these phenomena. Moreover, the amplitude that is significantly larger than the others coincides with the antenna that is transmitting at that specific interval of time. During sample frame tx_2 (the interval of samples between 5000 and 6000), the amplitudes of rx_2 are larger than those of the other receiver antennas. During these samples only tx_2 is active. This raises the suspicion that there exists coupling between the transmitter and receiver pairs of which the transfer is stronger than the transfer of the EM signals between the arrays.

The observed behavior of figure 5.4 affects the underlying techniques of spatial multiplexing. Table 5.1 shows the singular values with their respective condition ratios. Because a much stronger transfer exists between each of the receiver and transmitter antenna pairs than there exists between for instance tx_1 and rx_3, the coupling effectively induces a channel on its own. The channels induced by coupling are similar to the situation that would arise when the transmitters would have a loopback to the receivers. The found singular values will then be more or less equal, with low condition ratios as a result.

Table 5.1: Singular Values and condition ratios of the direct path experiment.

	1	2	3	4
SV	0.4463	0.3505	0.2913	0.1855
Ratio	1.0000	1.2731	1.5317	2.4054

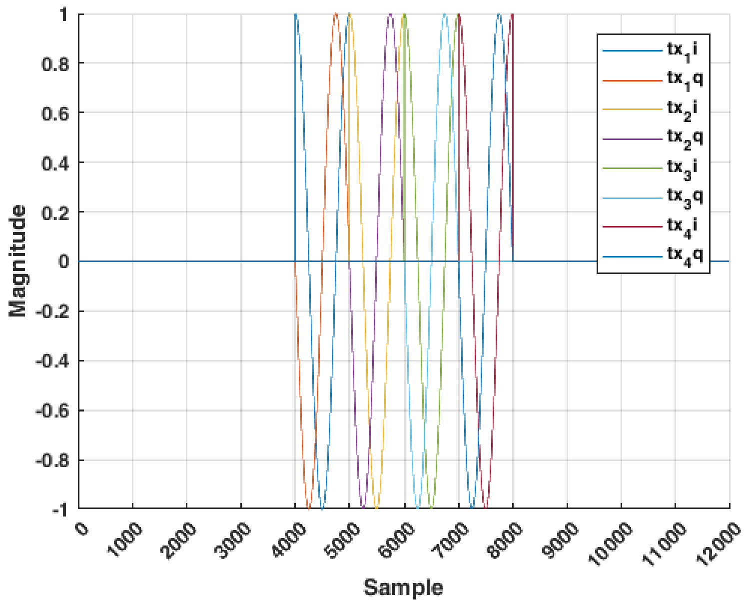

Figure 5.3: Plot showing the in-phase- and quadrature components of the transmitted pilot signals.

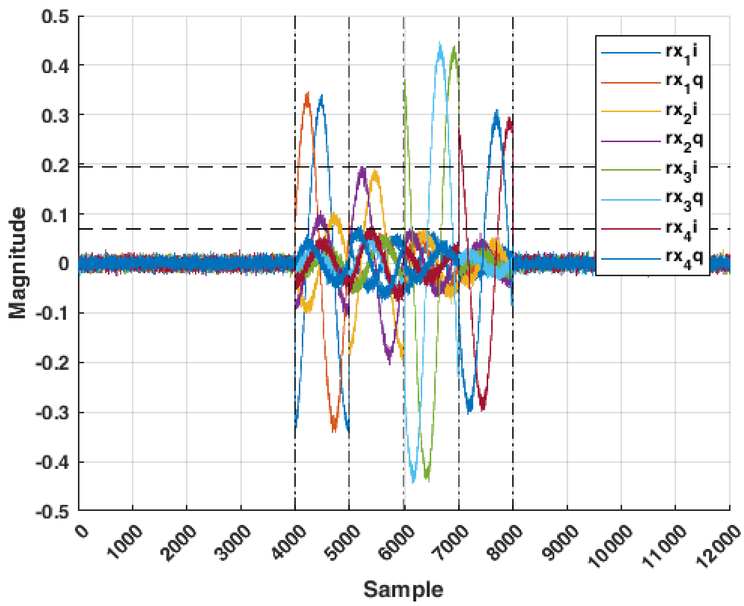

Figure 5.4: Received response on the pilot signals. The dot-dashed lines indicate the sample frames, the dashed lines indicate the maximum amplitudes of the received signals during the sample frame of tx_2 (5000-6000). It is shown that rx_2 has a larger amplitude than rx_1,rx_3 and rx_4.

Table 5.2 shows the singular values and condition ratios of the simulation for this experiment at similar noise levels. A comparison with the values of table 5.1 shows that something is off here, which is likely due to the on-chip coupling. While this situation is present, it is not useful to continue with the analysis of the results, as this would reflect only on the coupling behavior instead of spatial multiplexing.

Table 5.2: Singular Values and condition ratios of the direct path simulations.

	1	2	3	4
SV	0.1253	0.0179	0.0007	0.0003
Ratio	1.000	6.995	168.8	465.3

5.1.3 Conclusion

The results show that coupling occurs between each of the transmitter and receiver pairs. This coupling most likely originates in the traces of the Printed Circuit Board (PCB) of the FM-COMMS5 board. The transfer between each respective transmitter - receiver pair (for instance tx_2 and rx_2) is much larger than the transfer between other combinations of antennas (for instance $tx2$ and $rx4$). This would affect the working of spatial multiplexing and therefore has to be further investigated.

5.2 Coupling

In the experiment of section 5.1 unexpected behavior was observed. The hypothesis is that coupling occurs between the transmitter and receiver pairs on the PCB. The goal of this experiment is to establish whether the observed response is indeed caused by coupling and to find whether the effects of this coupling can be canceled.

5.2.1 Analysis

Figure 5.4 shows the results of a direct path measurement in the anechoic chamber. When comparing rx_3 with rx_1 and rx_2 for the samples of 6000 until 7000, it can be seen that the amplitude difference of the ADC output values is about seven times as high (0.06 for rx_1 and rx_2 compared to 0.42 for rx_3). The average maximum values for the non-coupled signals are roughly 0.03V (0.05 full scale input voltage). This is equivalent to a received power level of roughly -20dBm.

The amplitudes of the coupled signals range from 0.13V up to 0.28V (0.2 full scale input voltage to 0.44 full scale input voltage), which results in equivalent power levels of -7.5dBm up to -1dBm. With a transmitter power level of -2.5dBm and a receiver gain of 60dB, the loss of the non-coupled signals is found to be -77.5dB, which is much higher than the anticipated loss (equation 5.1). The transfer of the coupled signals is calculated to be $-1+2.5-60 = -58.5dB$ up to $-7.5+2.5-60 = -65dB$.

$$G_{path} = G_{Pathloss} + G_{Cableloss} + G_{S11} = -46.3 - 8.4 - 1.8 = -56.5dB \tag{5.1}$$

The datasheet [18][p6] lists an isolation of 50dB between the two receiver and transmitter channels of each AD9361 chip. Although this is the isolation from tx_1 to tx_2 and not the isolation of tx_1 to rx_1, the isolation of tx_1 to rx_1 is likely to be in the same range. An on chip

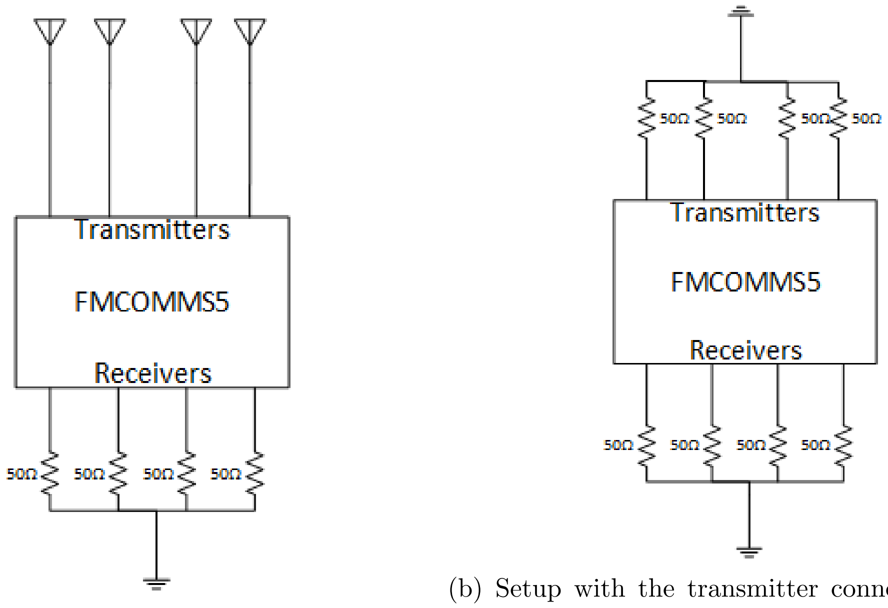

(a) Setup with the transmitter array connected.

(b) Setup with the transmitter connectors terminated.

Figure 5.5: The two setup configurations for the coupling experiments.

isolation of 60 dB between the transmitter and receiver channels would explain the observed coupling behavior. It does remain unclear why the uncoupled signals are 20dB weaker than anticipated.

For normal operations, a 50dB on chip isolation between various signals is sufficient. In the current case it is a problem because the actual desired signal is even weaker. In communication systems the transmitter and receiver are usually separated in space and therefore this problem would not occur. Also WiFi signals are in general half duplex and so the transmitter and receiver would not be active at the same time which also prevents coupling.

5.2.2 Method

To analyze the coupling, two setups will be used, see figures 5.5a and 5.5b. In the setup of figure 5.5a the receiver antennas are removed and replaced by 50Ω termination components. The transmitter array remains connected to the transmitters to mimic live operation in the best way possible. In the setup of figure 5.5b both the receivers and the transmitters are terminated by the 50Ω termination components. This experiment is carried out to see whether these termination components have any influence on the coupling itself.

There are no antennas connected to the receivers in either of these situations. If the only transfer from transmitter to receiver is through radio communication, there should not be any signal measured at the receiver. It is expected that there will be coupling within the PCB or inside the transceiver chip causing signals to appear in the measurements. It is also expected that these are dependent on both the frequency, the transmitter power level and the receiver gain. Therefore experiments will be carried out with varying levels of transmitter power and varying frequencies to test this hypothesis.

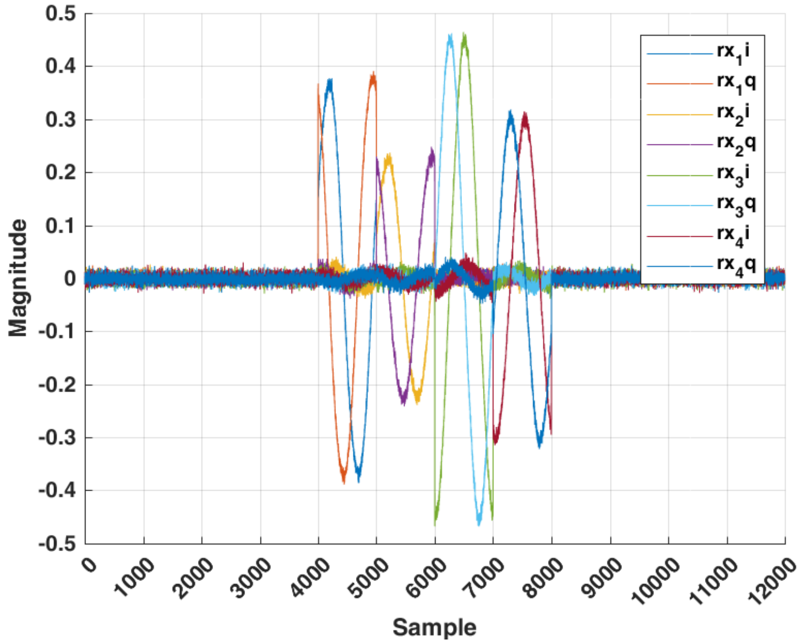

Figure 5.6: Sampled coupling signals using 10dB transmitter attenuation and 60dB receiver gain at 2.45GHz using termination components for the receiver connectors.

5.2.3 Results

Figure 5.6 shows the captured signals for the setup of figure 5.5a at a frequency of 2.45GHz, with 10dB transmitter attenuation and a receiver gain of 60dB[1].

It is observed that there is a transfer from transmitter to receiver even though the receiver has no antennas connected to it. It is also found that the coupling does not seem to be isolated to the respective channel pairs. Some coupling can be observed between tx_1 to rx_2 and also between tx_1 to rx_4, even though tx_1 is created by the first AD9361 chip and rx_4 is received by the second AD9361 chip.

Another assumption was that the coupling was linearly dependent on the transmitted power. Figure 5.7 shows the results from a situation in which the transmitter is attenuated by an additional 6dB. The complete configuration then lists a transmitter attenuation of 16dB and a receiver gain of 60dB at a frequency of 2.45GHz.

Figure 5.7 shows that the sampled amplitude is approximately half of that of figure 5.6. As the values shown are the sampled voltages of the ADC, this indeed corresponds to the 6dB additional attenuation in power. The most obvious solution, apart from separating the receiver from the transmitter, would thus be to reduce the transmitted power. This would linearly reduce the coupling effects while the actual transmitted signals could be amplified to desired power levels externally. This would require external amplifiers that are capable of operating at 2.45GHz.

Looking again at figure 5.7 it is also promising that the phases of the measurements seem to remain constant. This would open up the possibility to cancel the coupling. A calibration

[1]These settings are the same as the ones used in the experiment of section 5.1.

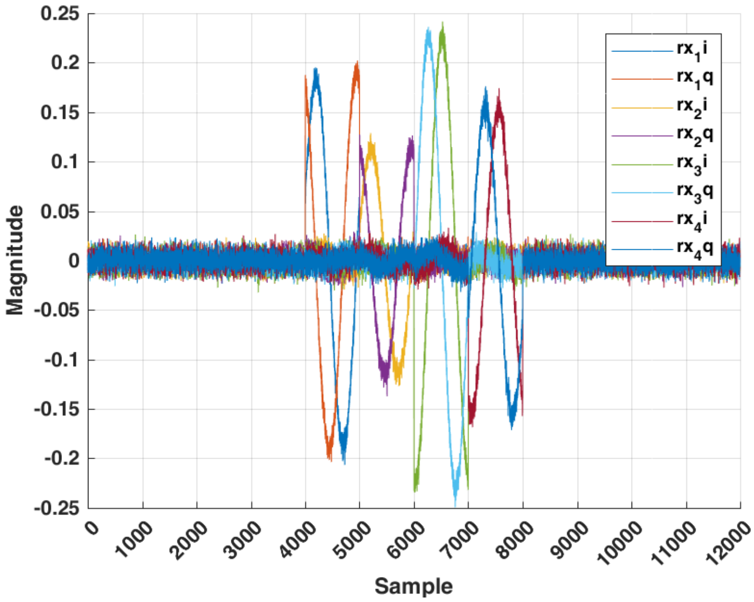

Figure 5.7: Sampled coupling signals using 16dB transmitter attenuation and 60dB receiver gain at 2.45GHz using termination components for the receiver connectors.

measurement could be taken without antennas, which could then be used to cancel the coupling during the actual experiments.

The transmitter antennas are now replaced with 50Ω termination components. The reasoning behind this is that if the coupling effects change, the coupling is likely to be dependent on the impedance that is connected to the SMA connector. If it is not, the coupling is likely to origin earlier in the transceiver chain. Figure 5.8 shows the result of replacing the antennas at the receiver and transmitter with 50Ω termination components.

Comparing figure 5.8 with figure 5.6 it is observed that the coupling effects have indeed changed. If the peak of the quadrature component is taken as a reference, the respective changes of tables 5.3 and 5.4 can be determined in the amplitude and phase.

Table 5.3: Locations and the values of the maximum amplitude for each channel for the two setups of figure 5.5. The row labeled 'Array' denotes the peaks for the setup of figure 5.5a and 'Terminated 50Ω' denotes the peaks for figure 5.5b.

	rx_1q		rx_2q		rx_3q		rx_4q	
	sample	value	sample	value	sample	value	sample	value
Array	4950	0.39	5943	0.25	6287	0.46	7293	0.31
Terminated 50Ω	4456	0.40	5442	0.24	6513	0.45	7559	0.32

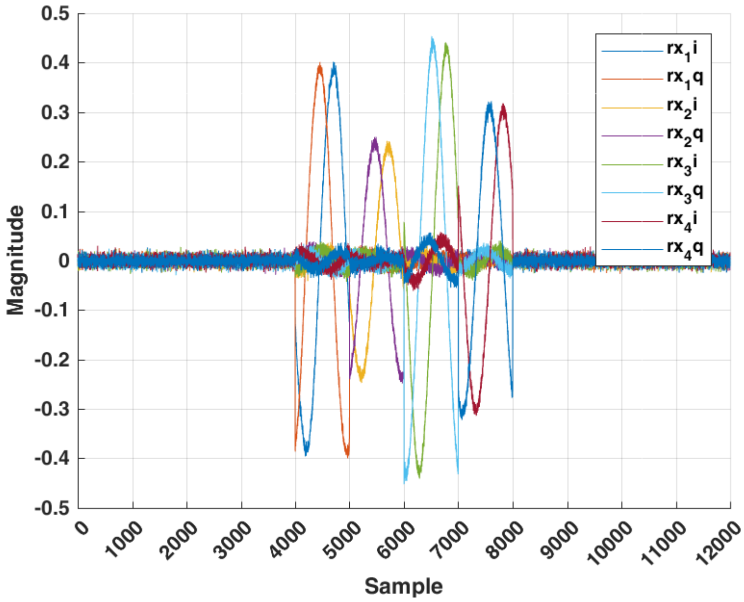

Figure 5.8: Sampled coupling signals using 10dB transmitter attenuation and 60dB receiver gain at 2.45GHz using termination components on both transmitter and receiver.

Table 5.4: Phase shifts of table 5.3 expressed in degrees instead of samples. Values shown are the phase shift for the setup of figure 5.5a with respect to the phase of the signals of the setup of figure 5.5b

	rx_1	rx_2	rx_3	rx_4
Phase difference	-182°	-179°	-81°	-96°

The results show that the amplitudes of the signals do not change much, but the phase does. This implies that it will be very difficult to cancel the coupling effects because they are not constant when changing the load. To be able to cancel the coupling, a calibration measurement should be carried out whilst both the arrays are connected and meanwhile preventing the broadcast signals to arrive at the other array. This would be practically impossible in any realistic situation.

Every measurement shown so far has been repeated three times in quick succession. These measurements show, apart from changes contributed to noise, no difference with respect to one another. However, figures 5.9 and 5.10 show what happens if the FMCOMMS5 board is temporarily disabled by setting the Enable State Machine (ENSM) mode to *sleep* and back to *fdd*[2] in between measurements.

From the results, it is observed that the amplitude has no significant change. The phase does show a significant change. Moreover, it shows the same behavior that was mentioned earlier when comparing the measurements of the setups of figures 5.5a and 5.5b. Earlier this behavior was contributed to a changing load, but it is apparently linked to the start-up behavior of the device.

An explanation for this behavior can be found in the block diagram of the AD9361 chip of

[2] *fdd* is the mode for standard operation.

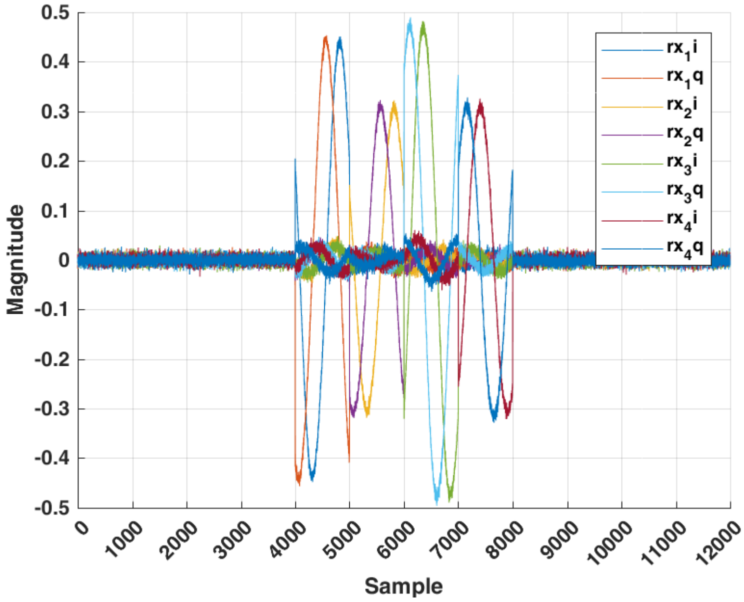

Figure 5.9: Coupling measurement after re-initiating the device for the first time.

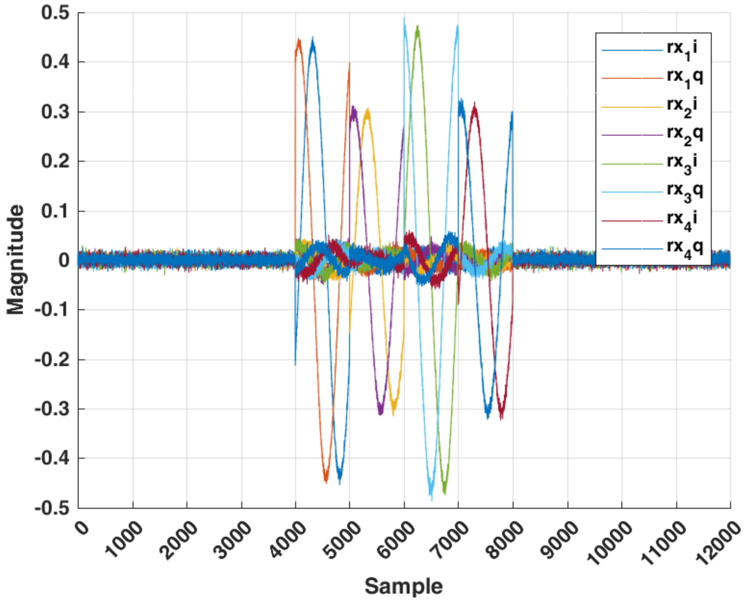

Figure 5.10: Coupling measurement after re-initiating the device for the second time.

figure 4.2. In the middle on the left the generation of the modulator signals is shown. Even though the signals are generated by the same crystal, the synthesizers that create the Local Oscillator (LO) signals used for modulation and demodulation are distinct devices[22][p18]]. This enables the simultaneous usage of the transmitter chain and the receiver chain at different frequencies. This, however, also implies that the LO signals are not guaranteed to be synchronized, with the result that after every synthesizer power-up there is an arbitrary phase difference between the two LO signals. This phase difference then causes a phase difference in the received signals.

To test this theory, the experiment is repeated with four loopback cables between each respective transmitter and receiver pair[3]. The results shown in figures 5.11 and 5.12 show that the phase difference also occurs in this situation. This troubles the ability to cancel the coupling effects as this phase difference has to be calibrated after every power-up sequence. A solution would be to use an external oscillator for the LO synthesizer signals. With the external oscillator used for both modulation and demodulation, there should not be variable phase shift anymore, as they are all performed by the same LO signal.

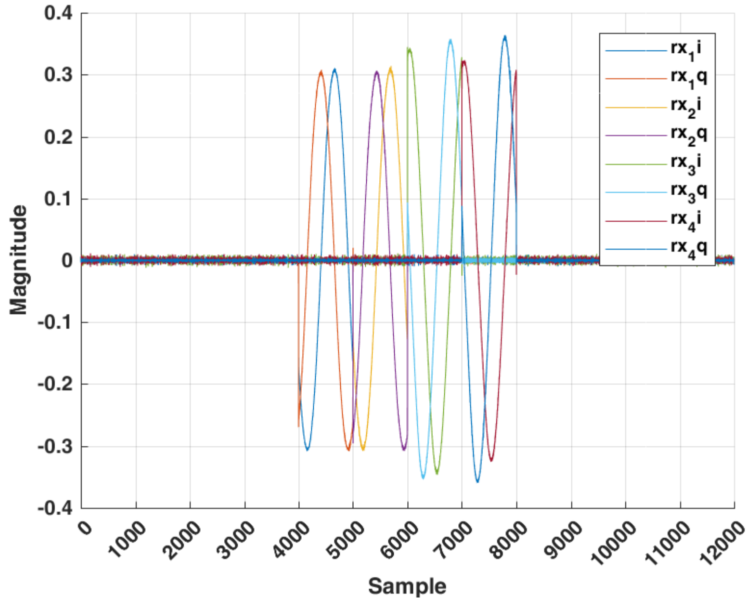

Figure 5.11: Measurement with loopback cables after booting up the first time.

[3]The receiver gain is set to 0dB to avoid clipping.

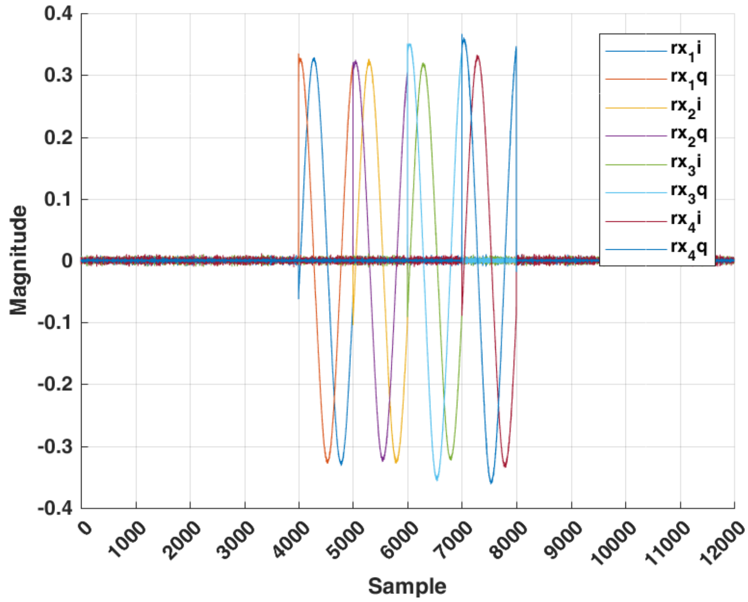

Figure 5.12: Measurement with loopback cables after rebooting the device.

Finally also the dependability on frequency has been looked into. Figures 5.13a, 5.13b and 5.13c show the response for the setup with both the transmitter and the receiver 50Ω terminated for frequencies of 800MHz, 2.45 GHz and 5GHz. The large differences in amplitude show that the coupling is also dependent on the frequency.

5.2.4 Conclusion

Experiments have shown that coupling occurs inside the PCB of the FMCOMMS5. The rejection of the PCB between the transmitter and receiver pairs is found to be inadequate for the purpose of the experiments. The rejection is estimated to be in the 50-60dB range. The complete path loss of the setup exceeds that, causing the coupling inside the PCB to be larger than the desired signals.

It was found that the design of the hardware made it too troublesome to obtain a situation where it was possible to cancel the coupling. The option of decreasing the transmitted power on the board is preferred. External amplifiers can then be used to achieve the desired power levels.

A lack of synchronization between the LO signals of the synthesizers introduces phase offsets to the signals. These offsets remain and will be taken into account by the system during the estimation of the channel. This will make the analysis of the singular vectors much more troublesome.

5.3 External amplification

The experiment of section 5.1 indicated that there were problems concerning coupling. The experiment of section 5.2 further illustrated this and presented solutions to remedy this issue. In this experiment the transmitted power of the transceiver board will be substantially decreased

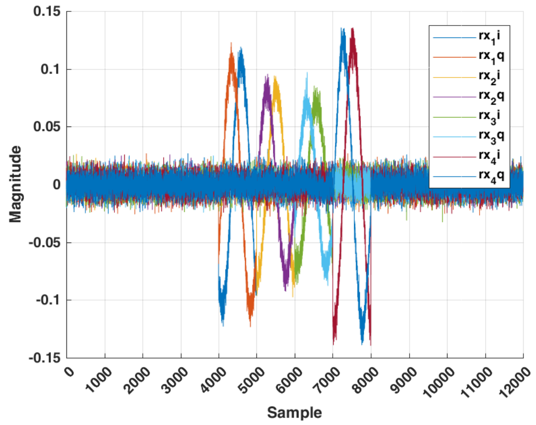

(a) Coupling results for a LO frequency of 800MHz.

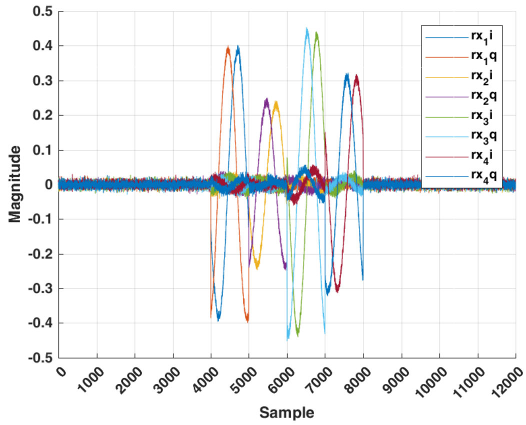

(b) Coupling results for a LO frequency of 2.45GHz.

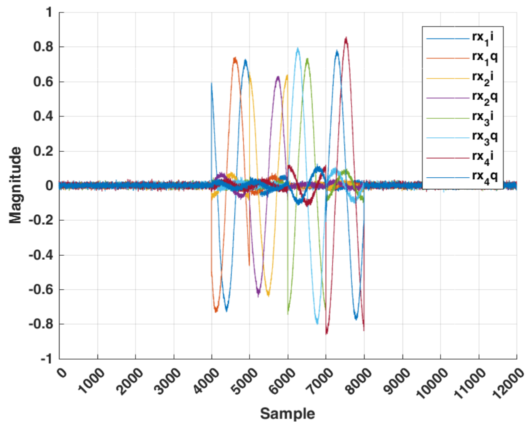

(c) Coupling results for a LO frequency of 5GHz.

Figure 5.13: Coupling effects for various frequency settings of the local oscillator.

and external amplifiers will be used.

The experiments will once again be carried out in the anechoic chamber and will have two goals. The first goal is to verify that the coupling effect has been decreased enough to do sensible measurements. The second goal of the experiment is to confirm the theories presented in chapter 2 by relating the simulations of chapter 3 to the processed results of the experiments.

5.3.1 Method

During the time of the experiments, the only amplifiers that were available, were the LNA-1440[23]. This Low Noise Amplifier (LNA) has an operating range of 10kHz up to 1400MHz. To be able to use these, the frequency of the LO signals has to be lowered to 1400MHz. Also a modification to the antenna array is required, as a linear phased array antenna works best with the antennas spaced at half a wavelength. Both the transmitter and receiver array are modified in such a way that the antennas are approximately 107mm apart, which coincides with half a wavelength at 1400MHz.

This modification also affects the measurements in the anechoic chamber. A decrease in frequency will increase the radius in which near field effects have to be taken into consideration. To be able to neglect near-field effects, the distance between the antenna arrays should be larger than $2D^2/\lambda$, where D is the largest dimension of the radiator and λ is the wavelength [24][p34]. The largest dimension of the array is the distance from tx_1 to tx_4 which is $3 \cdot 0.107m$. Equation 5.2 shows that after the modifications the receiver array is still spaced far enough to be considered in the far-field region.

$$R_{farfield} = \frac{2 \cdot 0.321^2}{0.107} = 1.92m \tag{5.2}$$

For the experiment the setup of figure 5.2 is used. The arrays are placed in the anechoic chamber at a distance of 2.9m from one another. Training signals are sent at a frequency of 1400Mhz with a transmitter power level of -42.5dBm (50dB attenuation). External amplifiers of the type LNA-1440 are used to provide a gain of 40dB. The experiments are all repeated four times for various situations. These situations vary with respect to the angle of the receiver array, the presence of reflective surfaces and the presence of an interferer. Because external amplification is required, the system platform is now placed outside the anechoic chamber. Both the transmitter and the receiver array are connected by SMA cables of six meters long.

5.3.2 Results

In figure 5.14 the resulting received signals are shown for the most basic setup possible. Only the two antenna arrays are present and neither of them is rotated (figure 5.2). Figure 5.14 shows that the signals received for each sample frame have roughly the same phase. This is the expected behavior when there is only a direct path between transmitter and receiver and the distance between every antenna pair is about the same.

It is also observed that during sample frame $tx2$ the signals are a bit weaker and messier than during the other sample frames. This is most likely caused by the fact that antenna tx_2 performs a bit worse than the other three. Ideally all the antennas should be calibrated for phase and amplitude characteristics to get a clear picture on this.

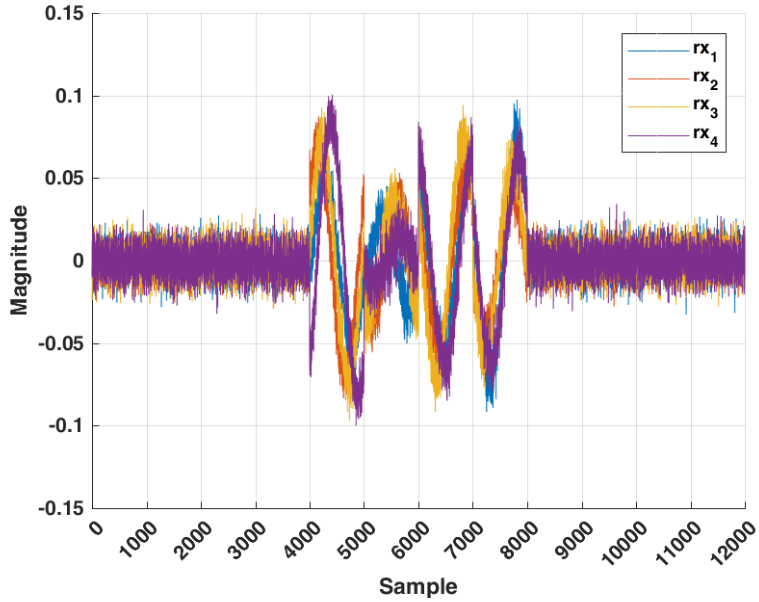

Figure 5.14: Received signals of a setup without any reflection surfaces added and both receivers 0° rotated.

More striking, however, is that sample frames tx_3 and tx_4 seem to have a phase offset of 180° compared to sample frame tx_2 and an offset of -90° with respect to sample frame tx_1.

The phase shift of tx_1 with respect to tx_3 and tx_4 can be explained by looking again at the synthesizers. Based on the experiment where the coupling between the transmitter and receiver pairs was investigated, it was mentioned that the built in synthesizers of each AD9361 chip for the transmitters and receivers are not phase locked. In figure 4.2 it is shown that this is also not the case for the synthesizer used for modulating tx_1 and tx_2 (AD9361_A) with respect to the synthesizer that is used for channels tx_3 and tx_4 (AD9361_B). A phase offset of 180° of the transmit synthesizer of AD9361_B with respect to AD9361_A, results in the pilot signals also having the same phase offset for the samples during the 6001-8000 interval.

This, however, does not explain the phase shift of sample frame tx_2. This transmitter is supposed to use the same LO signals for both modulation as demodulation as tx_1 and should therefore have roughly the same phase. It is most likely that the antenna tx_2 is not performing properly because the received amplitudes are also significantly smaller than during the other sample frames. This again does not impair the effects of spatial multiplexing (these offsets are take into account during training), but does complicate the analysis. This once again proves the need of a careful characterization of the antenna paths for a proper analysis.

As a comparison, figure 5.15 shows the simulation results for this scenario. Comparing the two figures, the actual measurements show a larger phase offset and larger amplitude difference compared to the simulations. The most likely explanation for this is the lack of calibration of each individual antenna that was discussed earlier.

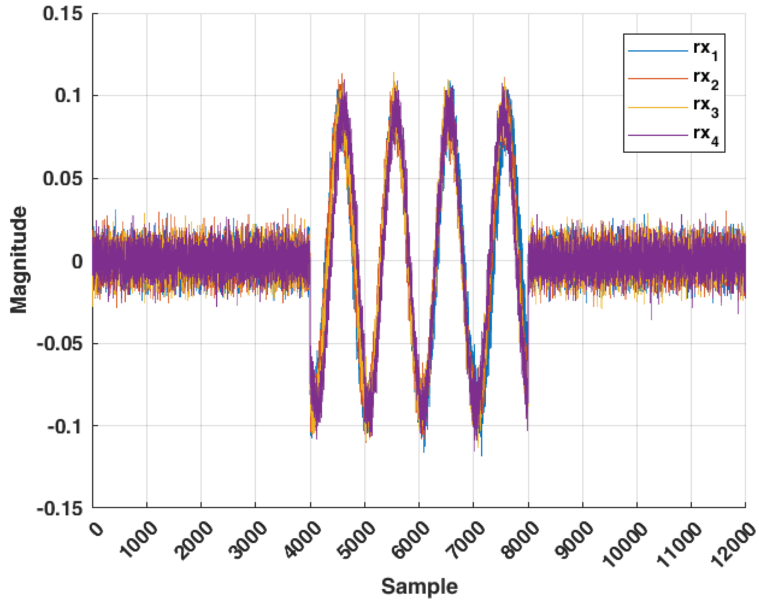

Figure 5.15: Simulated received signals of a setup without any reflection surfaces added and both receivers 0°rotated in an environment with with an SNR of 18dB.

Even though it will be difficult to interpret the spatial behavior (this is dependent directly on the phase characteristics of the antenna signals), it is still possible to analyze some aspects of the system. Using the measurements of figure 5.14 a channel estimation is performed by applying the least squares estimation of section 2.4.2. Table 5.5 shows the estimated matrix of the measurement results and table 5.6 shows the estimated matrix of the simulations.

Table 5.5: Estimation of the channel matrix for the measurement

0.052 ∠ 101°	0.027 ∠ 124°	0.054 ∠ -18°	0.074 ∠ -67°
0.069 ∠ 55°	0.037 ∠ -135°	0.052 ∠ -47°	0.042 ∠ -101°
0.073 ∠ 81°	0.036 ∠ -163°	0.072 ∠ -63°	0.058 ∠ -97°
0.083 ∠ 140°	0.014 ∠ -106°	0.064 ∠ -3°	0.062 ∠ -56°

Table 5.6: Estimation of the channel matrix for the simulation

0.089 ∠ -165°	0.091 ∠ -161°	0.090 ∠ -151°	0.089 ∠ -135°
0.090 ∠ -161°	0.089 ∠ -164°	0.090 ∠ -161°	0.089 ∠ -151°
0.089 ∠ -151°	0.090 ∠ -161°	0.089 ∠ -165°	0.090 ∠ -161°
0.089 ∠ -135°	0.090 ∠ -151°	0.090 ∠ -161°	0.091 ∠ -165°

These channel matrices do not display much new information in addition to figures 5.14 and 5.15. By comparing them it can be seen that the simulations roughly have the same power transfer as the experiment and that the phase differences between the antennas in each column vector are larger than in the simulations.

An SVD is performed on the estimated channel matrix. Table 5.8 shows the singular values and the respective condition ratios. Comparing these values to the ones that were obtained in the first experiment (with the unmodified array, see table 5.7) a clear distinction can be seen. A much larger decay is observable in the singular values. Table 5.9 shows the values from the simulation. It can be seen that the results for the experiments still do not get close to the benchmark figures of the simulation. This is also what you would expect as the simulation results are obtained with perfectly matched antennas in a perfect reflection-free environment.

Table 5.7: Singular Values and condition ratios of the direct path experiment at 2.45GHz without external amplification.

	1	2	3	4
SV	0.4463	0.3505	0.2913	0.1855
Ratio	1.0000	1.2731	1.5317	2.4054

Table 5.8: Singular Values and condition ratios of the direct path experiment at 1400MHZ with external amplification.

	1	2	3	4
SV	0.2201	0.0544	0.0313	0.0063
Ratio	1.0000	4.0464	7.0276	34.673

Table 5.9: Singular Values and condition ratios of the direct path simulations at 1400MHz.

	1	2	3	4
SV	0.3550	0.0515	0.0025	0.0002
Ratio	1.000	6.893	142.1	1599

Earlier it was explained that the left- and right singular vectors play a key role in spatial multiplexing. Figures 5.16a and 5.16b Show the angular sensitivity plots when these are used as steering vectors

Figure 5.16a shows the left singular vectors, which are used as steering vectors for the receiving array. The strongest gain is expected to be at 0° for both the transmitter and the receiver as the arrays are directed right at one another, Figure 5.16a shows indeed a strong gain in the direction of 0° for the first vector, which corresponds to the strongest singular value and thus the best path. This is also a logical result as the phases of the individual receiver antennas of figure 5.14 do not differ much from one another. To get constructive interference, the phase should be left unchanged which is indeed what happens when the steering angle is set to 0°,

The first right singular vector should also show a strong gain at 0°. Figure 5.16b shows that this is not the case, as the strongest gain is located at 20°. The explanation for this can be traced back to the phase offsets of figure 5.14 between each of the transmitter antennas. The signals from antenna tx_1 arrive at a different phase than the ones from antenna tx_4 during training. The signals fed to the transmit channels should thus be given different phase offsets to achieve a coherent wavefront at the receiver, which is the observed behavior of ev1 of figure 5.16b.

To further illustrate this behavior, figures 5.17a and 5.17b show the resulting angular sensitivity plots for the simulations. If for this simulation the transmit channels are given phase shifts which are similar to the ones observed in figure 5.14, the angular sensitivity plots change into the ones shown in figure 5.18. These figures show the same behavior as the experiment results. The left singular vectors hardly change, but the right singular vectors are compensating for the phase offset in the transmitter antennas. This results in the maximum gain for the right

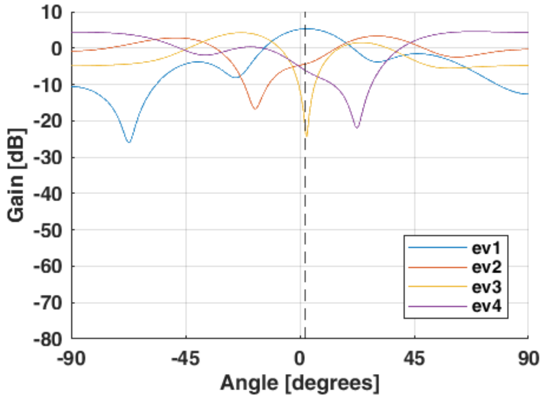

(a) Left singular vectors, **U**.

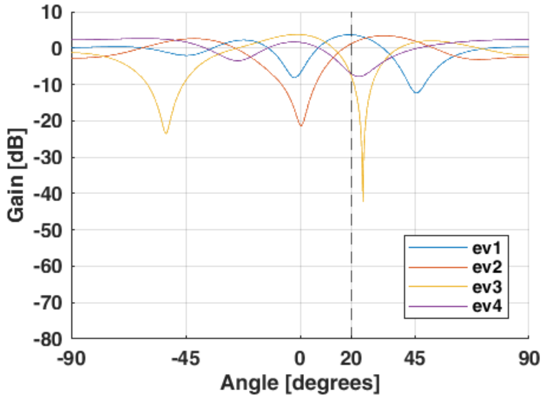

(b) Right singular vectors, **V***.

Figure 5.16: Directional sensitivity of the singular vectors for the experiment results. The dashed lines indicate the maximum gain of the first singular vector (ev1).

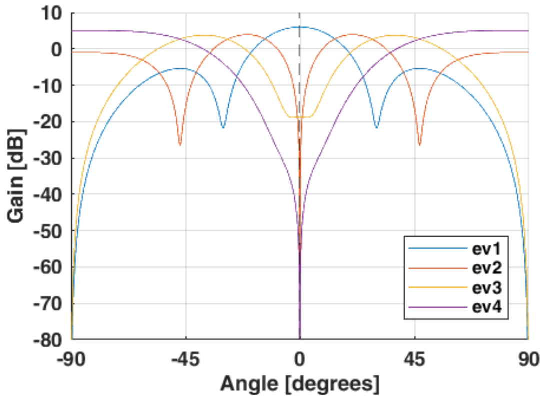

(a) Left singular vectors, **U**.

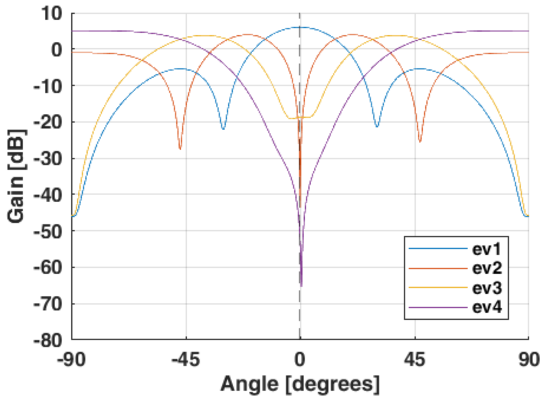

(b) Right singular vectors, **V***.

Figure 5.17: Directional sensitivity of the singular vectors for the simulation results. The dashed lines indicate the maximum gain of the first singular vector (ev1).

singular vector of the strongest singular value to shift from 0° towards 22°. In the same manner the measured signals could in theory be altered to shift the peak of the experiment results back to 0°. However, this requires a calibration of the phase offsets in the transmitter antennas which has not been performed.

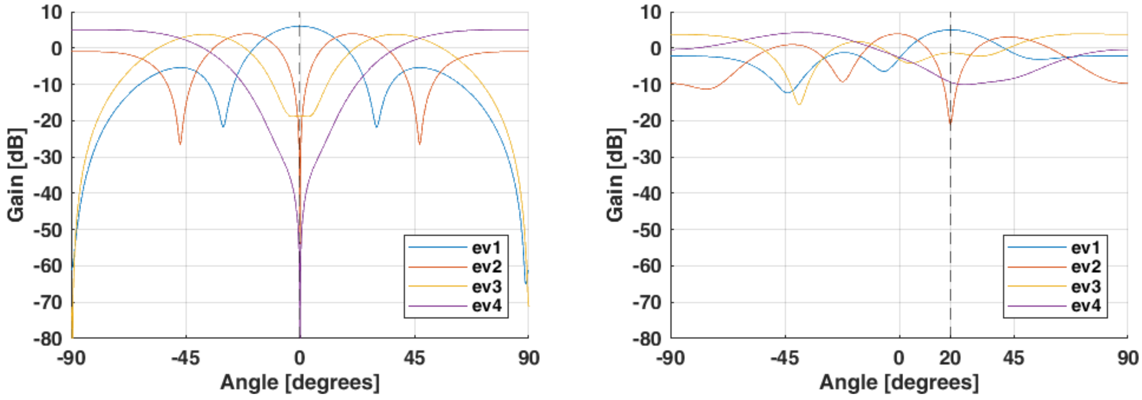

(a) Left singular vectors, **U**.

(b) Right singular vectors, **V***.

Figure 5.18: Directional sensitivity of the singular vectors for the simulation results with an individual phase offset introduced to the transmitter antennas. The dashed lines indicate the maximum gain of the first singular vector (ev1).

Rotated receiver array -30°

The experiment is repeated with the receiver array rotated by -30°[4]. This should result in a change of the left singular vectors, as these characterize the receiver array. As the transmitter is not altered, it is expected that the right singular vectors hardly change. Small changes are expected for the singular values. When the receiver array is at an angle, shadowing effects start to occur, which cause the received power to decrease.

Tables 5.10 and 5.11 show the singular values from the measurements, as well as the expected singular values from the simulations. Compared to the values from the experiment with the receiver at 0° the second singular value has become somewhat stronger and the third somewhat weaker, but overall the values lie in the same range.

Table 5.10: Singular Values and condition ratios of the direct path experiment at 1400MHZ with external amplification and the receiver array rotated -30°.

	1	2	3	4
SV	0.1866	0.0572	0.0210	0.0129
Ratio	1.0000	3.2601	8.8712	14.4258

Table 5.11: Singular Values and condition ratios of the direct path simulation at 1400MHZ with external amplification and the receiver array rotated -30°.

	1	2	3	4
SV	0.3560	0.0451	0.0018	0.0002
Ratio	1.0000	7.896	198.1	1447

When considering the right singular vectors (figure 5.19b) the same behavior is observed as before. The maximum gain of the strongest right singular vector is still shifted to about 20°. During these experiments the board has not been powered down. The same phase offsets as

[4]The setup did not have any means of measuring the exact angle of the array. Even though it says 30°, it might have very well been 20°or 40°as this was done by hand.

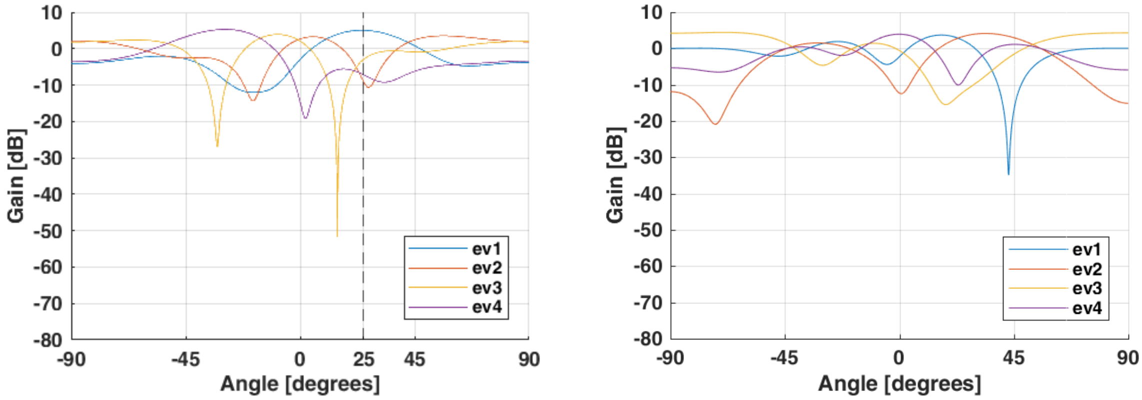

(a) Left singular vectors, **U**. (b) Right singular vectors, **V***.

Figure 5.19: Directional sensitivity of the singular vectors for the experiment results. The receiver array is rotated -30°. The dashed lines indicate the maximum gain of the first singular vector (ev1).

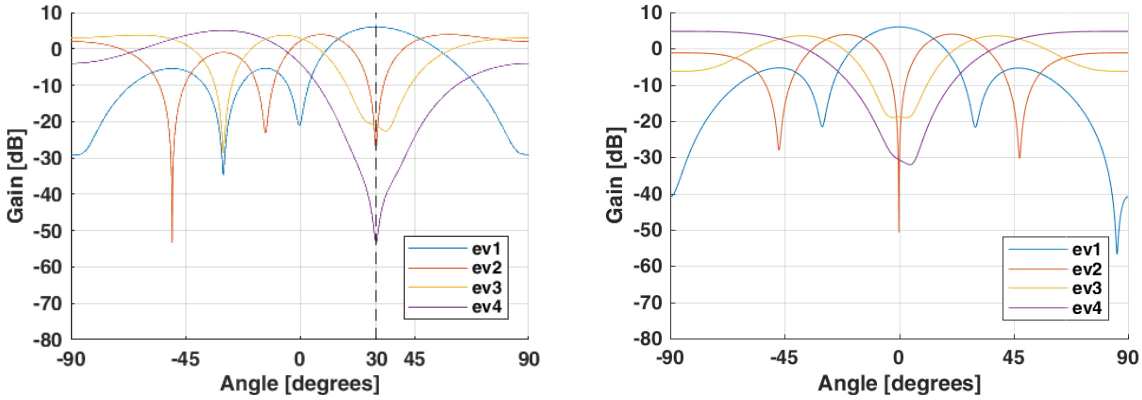

(a) Left singular vectors, **U**. (b) Right singular vectors, **V***.

Figure 5.20: Directional sensitivity of the singular vectors for the simulations. The receiver array is rotated -30°. The dashed lines indicate the maximum gain of the first singular vector (ev1).

before should therefore be still present, making this is an expected result.

In figure 5.19a it is observed that the directional sensitivity of the left singular vectors has changed. The maximum gain of the vector which corresponds to the first singular value (ev1) is no longer located at 0°, but has moved to 25°. It is also promising that there is a local minimum for the second vector (ev2) at about 27°. It shows that the system tries to reject the power from this angle for the second eigenmode. Figure 5.20 shows the directional sensitivity of the singular vectors from the simulations, which shows the same behavior (albeit stronger and at 30°).

Creating a secondary path

By introducing a piece of carton wrapped in aluminum foil, a reflective surface was added to the anechoic chamber. Figure 5.21 illustrates the setup in which the receiver array is still rotated

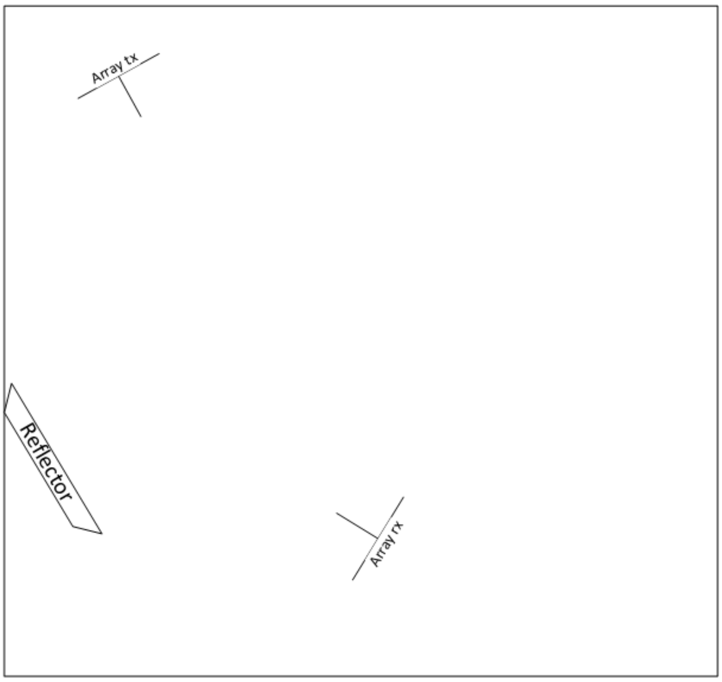

Figure 5.21: Orientation of the antenna arrays with a reflective surface added.

-30°. The sheet of reflective material should induce a reflection inside the anechoic chamber. The theory is that this reflection creates a secondary path from transmitter to receiver. The SVD is therefore expected to result in two relatively strong singular values, instead of just one.

Table 5.12 shows the resulting singular values for this setup. It is observed that the second singular value went up from 0.057 up to 0.092. Also the third singular value went up quite a bit. This could either mean that the reflective layer somehow created more than a single additional path, or that the second singular value of the previous experiment was caused by for instance a mismatch in the antennas and that the second singular value of the previous experiment is now present as the third singular value.

Again a simulation is performed of the experiment for comparison. In table 5.13 the simulation results are shown. When comparing these values, the results from the experiment seem plausible. The secondary path via the reflector is a little worse than expected and the third and fourth singular values are a bit stronger than anticipated, something that has been observed in all the results so far. Once again it is stressed that the simulation is only a crude approximation of the reality, it does not take into account defects in the antenna arrays and also assumes a perfect reflector. Also the location and the angles of both the arrays and the reflector do not exactly match the ones from the simulations.

Table 5.12: Singular Values and condition ratios of the experiment at 1400MHz with external amplification and the receiver array rotated -30°. An additional reflective surface has been added to the room at -45 degrees.

	1	2	3	4
SV	0.1890	0.0923	0.0363	0.0074
Ratio	1.0000	2.0483	5.2057	25.539

Table 5.13: Singular Values and condition ratios of the simulation at 1400MHz with external amplification and the receiver array rotated -30°. An additional reflective surface has been added to the room at -45 degrees.

	1	2	3	4
SV	0.3946	0.2092	0.0372	0.0075
Ratio	1.0000	1.8857	10.609	52.641

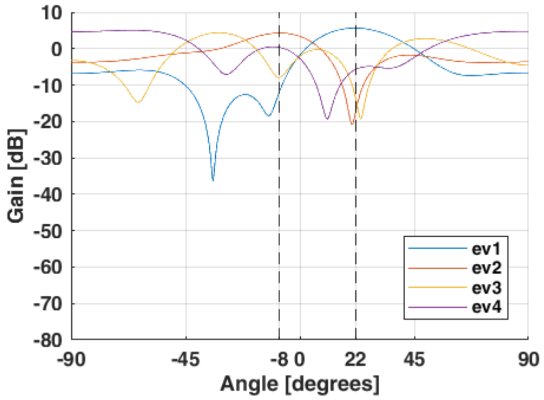

(a) Left singular vectors, **U**.

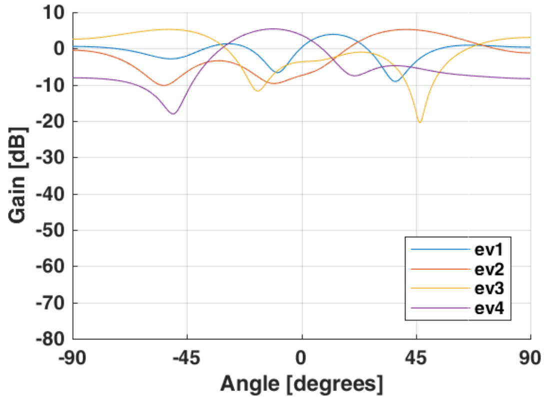

(b) Right singular vectors, **V***.

Figure 5.22: Directional sensitivity of the singular vectors for the experiment results. The receiver array is rotated -30° and with a reflector added at an angle of -45°. The dashed lines indicate the maximum gain of the first (ev1, 22°) and second singular vector (ev2, -8°).

When looking at the resulting singular vectors of figures 5.22a and 5.22b, it is observed that the left singular vector corresponding to the secondary path (ev2) has shifted a bit to the left to about -8°. When looking at figure 5.21, this is close to the angle from which one would expect the reflected signals to come from. The facts that the second singular value has increased and that the corresponding left singular vector has shifted towards the anticipated angle of arriving, indicate that the second path has successfully been identified by the system.

Just as a reference, figures 5.23a and 5.23 give the directional sensitivity plots of the singular vectors for the simulations. The peaks of both *ev1* and *ev2* seem to align to some extent, but because of the crude approximations, it is hard to give decisive statements about these figures.

5.3.3 Conclusion

The first goal of this experiment was to verify that coupling no longer affected the system. With the modified setup, all the receiver antennas were at roughly the same power level, which was not observed before. In addition to that, the singular values were also much closer to the expected values of the simulations. In that sense the problem has been resolved successfully.

The second goal of this experiment was to address whether the operation of the spatial multiplexing techniques could be verified by physical experiments. During the experiments it was observed that the behavior in the system could be linked back to the theory to some extent.

The lack of good calibrations for each of the transmitter and receiver channels (the interface, the cable and the antenna) proved troublesome. The synthesizers used for modulation

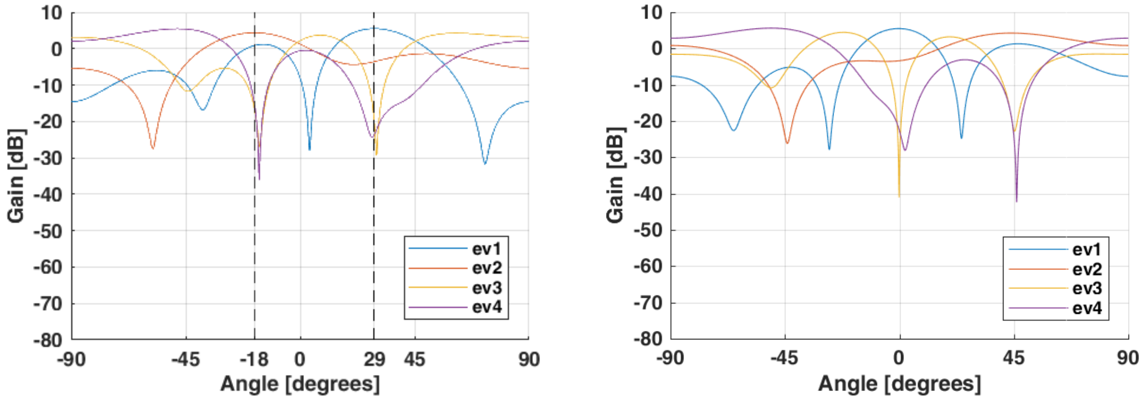

(a) Left singular vectors, **U**. (b) Right singular vectors, **V***.

Figure 5.23: Directional sensitivity of the singular vectors for the simulations. The receiver array is rotated -30°.

and demodulation are not synchronized and cause a phase offset in the transmitters for at least some measurements. This could only be deduced from the first experiment with only a direct path present (here it is easy to spot because all the signals are meant to have the same phase). To avoid this problem, either external LO signals have to be used, or the channels need to be calibrated after power-up of the board and before the measurements.

5.4 Practical environment

The experiments of section 5.3 were performed in an anechoic chamber. This is useful when the goal is to verify the correct behavior of the system. The eventual goal is to operate the system in an arbitrary environment. This is why also some experiments are carried out in a common lab room. An impression of the new situation is given in figure 5.24.

As the setup is no longer in an anechoic chamber, not even the simplest case can indicate the phase offsets caused by the synthesizers. This makes it impossible to say anything useful about the singular vectors as it is unknown whether these take a phase offset into account and if they do, what that offset is. The singular values are however unaffected by this and can be interpreted normally.

Figure 5.25 shows the measured signals at the receiver array when the experiment is performed in this room. Both the arrays are directed at one another (0° rotated), the transmitter power is set to -2.5dBm and the receiver gain is set to 60dB. The measurements are still performed at a frequency of 1400MHz.

A comparison of figures 5.25 and 5.14 shows that the received power levels are different. Even though the distance of both setups was the same (give or take a few centimeters), the sampled voltage of the ADC's has more than doubled compared to the experiment in the anechoic chamber. The additional received power can be explained by the reflections in the room. As can be seen in figure 5.24, the receiver array is next to a row of metal cabinets, which should reflect the EM waves very well.

This is also evident from the singular values which are shown in table 5.14. The singular

Figure 5.24: Photo taken from the setup in a common lab environment.

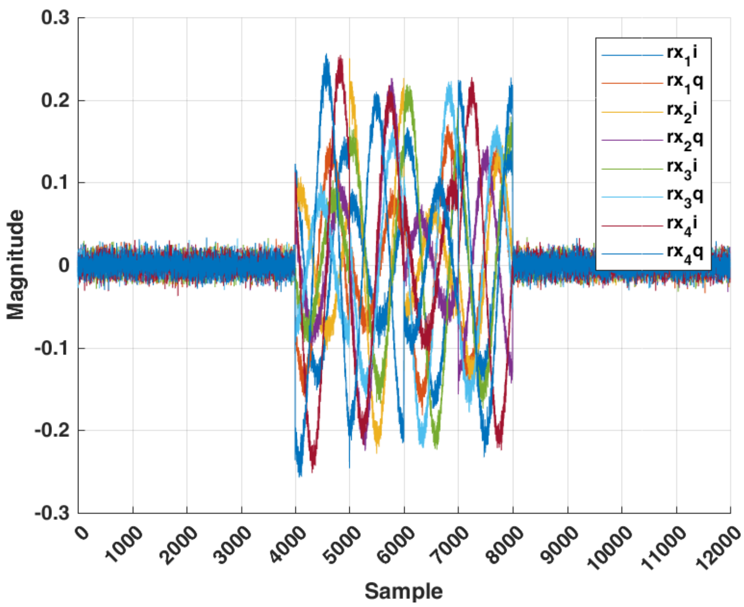

Figure 5.25: Measured signals at the receiver array in a common laboratory.

values are much larger than the ones found earlier, which also shows the increase of received power. The ratio between the singular values is also interesting. the second singular value is only 11% lower than the first singular value, indicating that the secondary path would perform almost equally well compared to the primary path. The fact that also the third and fourth singular values are quite large, indicate that this is a rich scattering environment which is very suitable for spatial multiplexing.

Table 5.14: Singular Values and condition ratios of the experiment at 1400MHz in a laboratory. Both the receiver array as the transmitter array are directed right at one another.

	1	2	3	4
SV	0.4377	0.3876	0.1523	0.0904
Ratio	1.0000	1.1291	2.8739	4.8426

For the sake of completeness figures 5.26a and 5.26 show the angular sensitivity of the singular vectors in a common laboratory environment.

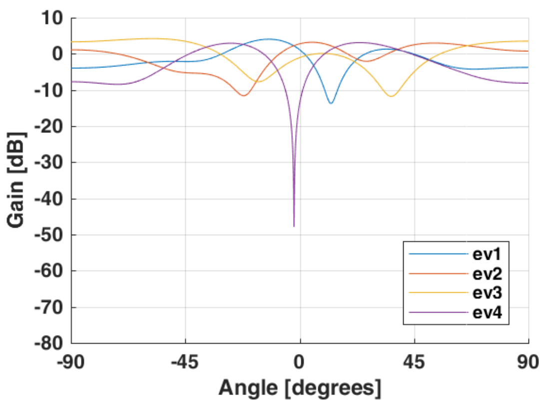

(a) Left singular vectors, **U**.

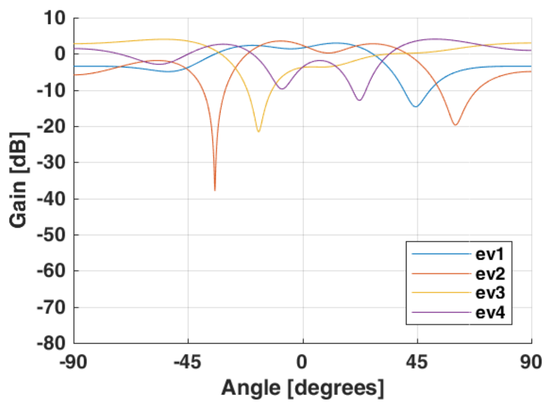

(b) Right singular vectors, **V***.

Figure 5.26: Directional sensitivity of the singular vectors for the experiment in a practical situation. The arrays are placed in a common laboratory room and are directed towards one another.

Chapter 6

Interference Suppression

In section 2.7, a method of interference suppression was presented. In this chapter both simulations and experiments will be performed to see the advantages and the shortcomings of the proposed technique.

6.1 Simulations

To illustrate the concepts of the interference suppression technique, the simulated setup of figure 6.1 will be used. By using the system model that was discussed in section 3, the expected received signals can be determined when the pilot sequence is transmitted (figure 6.2).

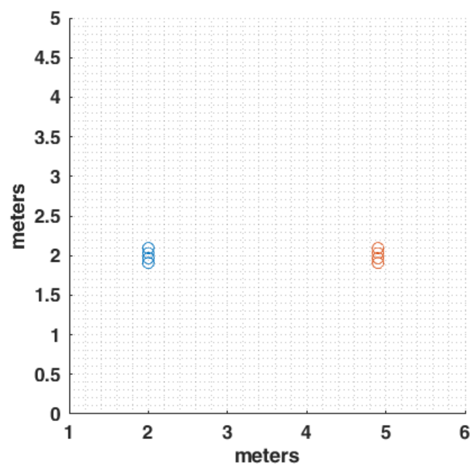

Figure 6.1: The floor plan of the setup

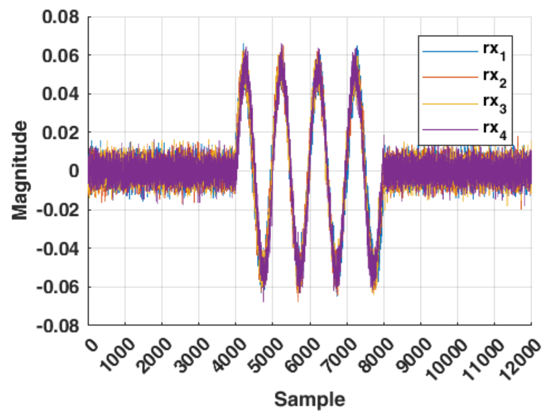

Figure 6.2: The expected received signals at the receivers for the case without interference

In addition to the received signals from the direct path, interference will be introduced to the received signals. The interference is a continuous sine wave originating from 45° with respect to the receiver array. Figure 6.3 shows the interference by itself and figure 6.4 shows the received signals when distorted by the interference.

To make a profile of the interference, a measurement has to be performed without any of the system's own transmitters active. The signals of figure 6.3 can be used for this. The eigenvalues

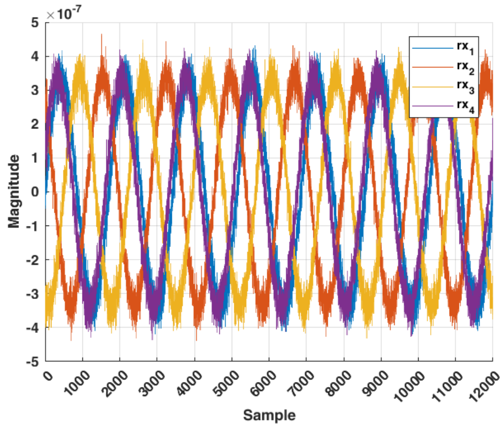

Figure 6.3: The simulated interference signal plotted with noise present.

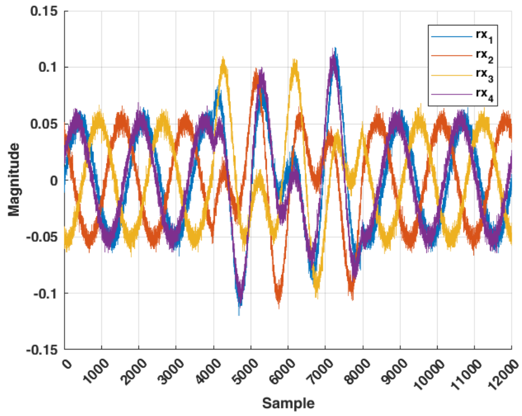

Figure 6.4: Response of the direct path simulation with the interference present.

(**D**) and eigenvectors (**V**) are determined and the MUSIC algorithm is applied with a noise subspace of three dimensions. The result is the MUSIC spectrum as shown in figure 6.5. The found eigenvectors and eigenvalues are shown in tables 6.1 and 6.2

Table 6.1: Eigenvectors of the covariance matrix of the interference profile measurement.

0.303 ∠ -31°	0.772 ∠ -6°	0.250 ∠ 140°	0.499 ∠ 22°
0.648 ∠ 114°	0.323 ∠ -9°	0.475 ∠ -163°	0.500 ∠ -106°
0.666 ∠ -152°	0.114 ∠ -73°	0.542 ∠ 147°	0.500 ∠ 127°
0.209 ∠ 0°	0.535 ∠ -180°	0.647 ∠ -180°	0.501 ∠ 0°

Table 6.2: Eigenvalues of the covariance matrix of the interference profile measurement. Values shown are $\cdot 10^{-12}$.

0.0057	0	0	0
0	0.0058	0	0
0	0	0.0059	0
0	0	0	0.4674

Figure 6.5 shows a peak value at -45°. This indicates that the MUSIC algorithm has isolated the signal subspace to which the interference belongs. As was discussed before, the eigenvectors can be interpreted as steering vectors. Of these eigenvectors the first three will be based on white Gaussian noise. The last eigenvector spans the signal subspace of the interference. It is expected that the first three subspaces show a null at -45° and that the last eigenvector shows a large peak at -45°. In figure 6.6 a directional sensitivity plot is given of all the four eigenvectors showing this behavior.

If the fourth eigenvector is removed from **V**, the transformation matrix **F** is created. To comply with the dimensions of the received signals **Y**, the Hermetian transpose is taken of **F** and the matrix is left multiplied by **F** itself, with the spatial filter $\mathbf{FF}^*$ as a result. Table 6.3 shows the resulting matrix of ($\mathbf{FF}^*$). The matrix is constructed in such a way that for each column, destructive interference occurs for the angle of incidence of the interferer. This

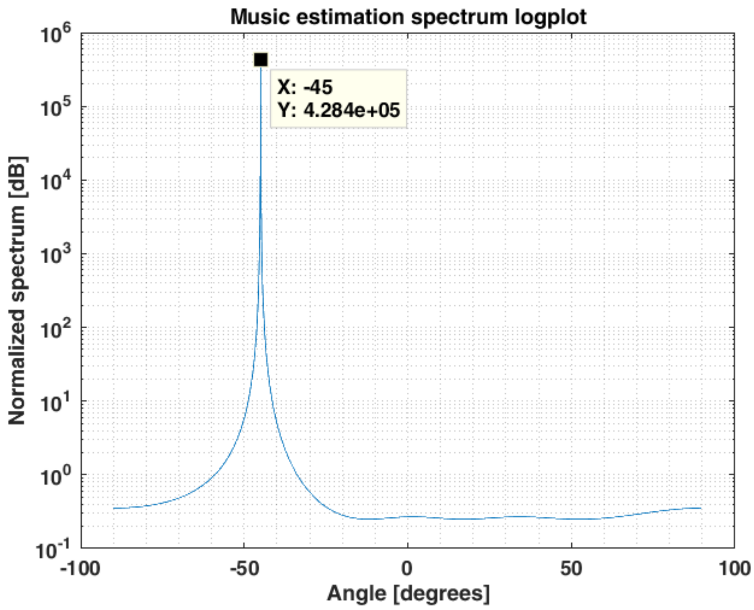

Figure 6.5: Results of the MUSIC algorithm using three noise subspace dimensions.

behavior becomes more clear when the interferer signal has an incident angle of 0° (the phase of the interferer signal is the same on each receiver antenna). Table 6.4 shows the values of ($\mathbf{FF}^*$) for an incident angle of 0°. For every vector, a linear combination of three of its components cancel the contribution of the fourth component (the one on the diagonal of the matrix).

Table 6.3: The values of the spatial filter matrix ($\mathbf{FF}^*$) for an interferer with an incident angle of -45°.

0.751 ∠ -0°	0.250 ∠ -53°	0.249 ∠ 74°	0.250 ∠ -158°
0.250 ∠ 53°	0.750 ∠ -0°	0.250 ∠ -53°	0.251 ∠ 74°
0.249 ∠ -74°	0.250 ∠ 53°	0.750 ∠ -0°	0.250 ∠ -53°
0.250 ∠ 158°	0.251 ∠ -74°	0.250 ∠ 53°	0.749 ∠ -0°

Table 6.4: The values of the spatial filter matrix ($\mathbf{FF}^*$) for an interferer with an incident angle of 0°.

0.750 ∠ -0°	0.250 ∠ 180°	0.250 ∠ -180°	0.250 ∠ -180°
0.250 ∠ -180°	0.749 ∠ -0°	0.250 ∠ -180°	0.250 ∠ -180°
0.250 ∠ 180°	0.250 ∠ 180°	0.750 ∠ -0°	0.250 ∠ 180°
0.250 ∠ 180°	0.250 ∠ 180°	0.250 ∠ -180°	0.750 ∠ -0°

The filtering behavior can also be shown graphically when the spatial filter matrix ($\mathbf{FF}^*$) is regarded as a matrix containing steering vectors. Figure 6.7 shows the angular sensitivity plot of ($\mathbf{FF}^*$). It shows a strong rejection at -45°, which is desired as that is where the interference is coming from. It is however important to note what happens at the other angles, as these angles might hold actually desired information later.

It can be seen that at 0° *ev2* and *ev3* are about 3 and 5 dB stronger than *ev1* and *ev4* respectively. This shows that the filter does have an effect on the amplitudes (and probably

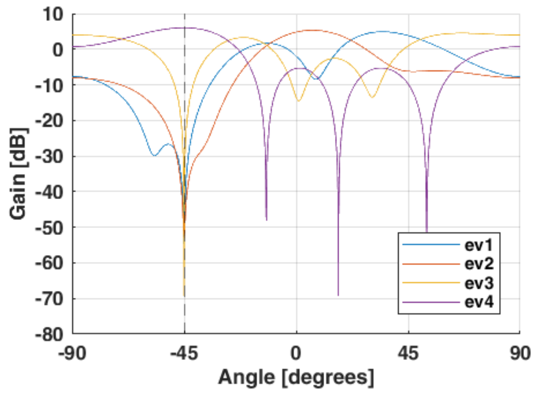

Figure 6.6: Directional sensitivity of the eigenvectors of the covariance matrix of the callibration measurement. ev1 through ev3 depict the noise subspaces and ev4 depicts the signal subspace of the interferer.

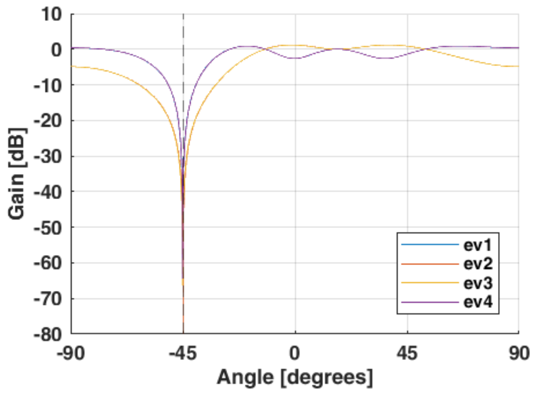

Figure 6.7: Directional sensitivity of the spatial filter $\mathbf{FF}^*$.

also the phase) of the signals at other angles. This may seem worse than it actually is. All these operations are performed before estimating the channel. When the received pilot signals during estimation of the channel matrix are processed by the same spatial filter, these effects will be taken into account and assumed to be part of the channel. The SVD will then automatically adjust itself accordingly.

Figure 6.8 shows the response when the signals of figure 6.4 are filtered by the spatial filter using equation 6.1. In this figure the interference has successfully been removed. Also it is observed that rx_1 and rx_2 have indeed been weakened by the filter by the ratios that were given earlier.

$$\mathbf{Y}_{\mathbf{filtered}} = (\mathbf{FF}^*)\mathbf{Y} \tag{6.1}$$

It may seem odd that there are no other visible alterations to the result other than a slight phase shift and some modified amplitudes of the signals. The filter was constructed by taking four eigenvectors and removing one of them. The rank of $(\mathbf{FF}^*)$ therefore has been reduced from four to three. The resulting matrix $\mathbf{Y}_{\mathbf{filtered}}$ also has a reduction of its rank compared to $\mathbf{Y}$, but this is not visible in figure 6.8.

Using the filtered signals it is possible to perform a channel estimation and a singular value decomposition. Table 6.5 shows the resulting singular values and the ratios between them. It shows that the fourth singular value is a factor 10^{16} smaller than the first singular value. This shows that a dimension has been sacrificed to filter the interference out.

Table 6.5: Singular Values and condition ratios of the simulation after filtering the received signals.

	1	2	3	4
SV	0.2181	0.0213	0.0004	$1.4 \cdot 10^{-15}$
Ratio	1.0000	10.206	617.36	$1.5 \cdot 10^{16}$

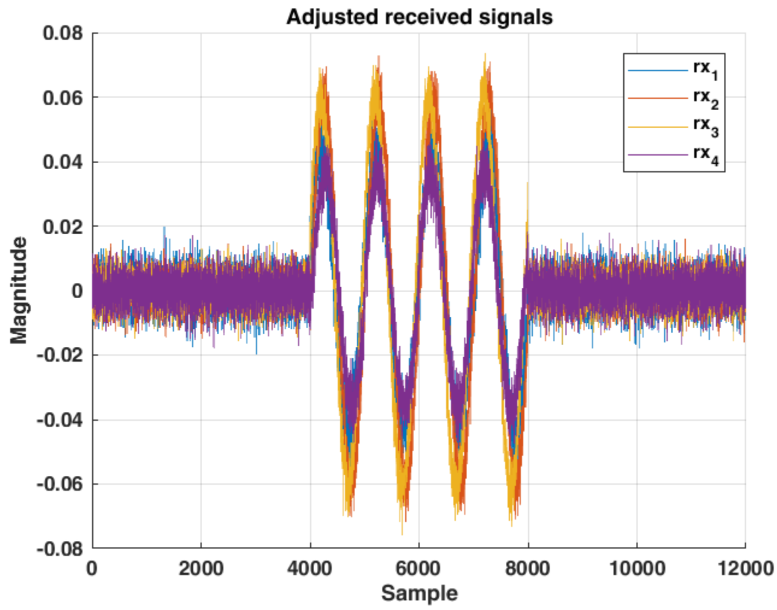

Figure 6.8: The received signals after multiplication with the spatial filter $\mathbf{FF}^*$.

Directional sensitivity plots can again be created for the left- and right singular vectors (See figures 6.9 and 6.10). It is shown that there is a null at -45° for the first three left singular vectors. Only the fourth left singular vector has a peak there, but as the corresponding singular value is so small, this vector will never be used. As a comparison, the directional sensitivity plots of the situation without interference and filtering are shown in figures 6.11 and 6.12.

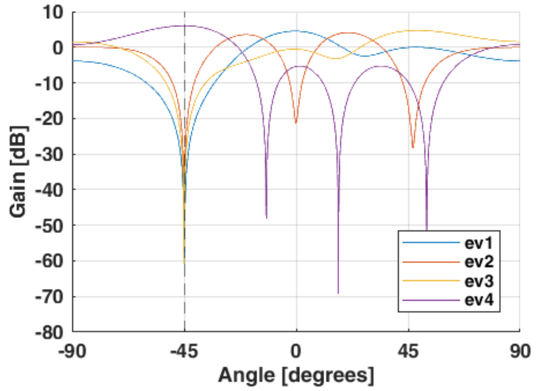

Figure 6.9: Directional sensitivity of the left singular vectors after filtering. The dashed line indicates the angle for which the spatial filter is tuned.

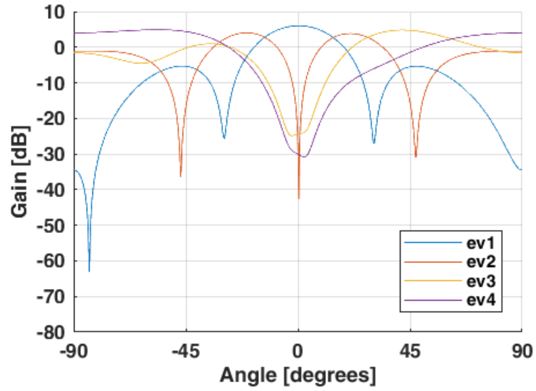

Figure 6.10: Directional sensitivity of the right singular vectors after filtering.

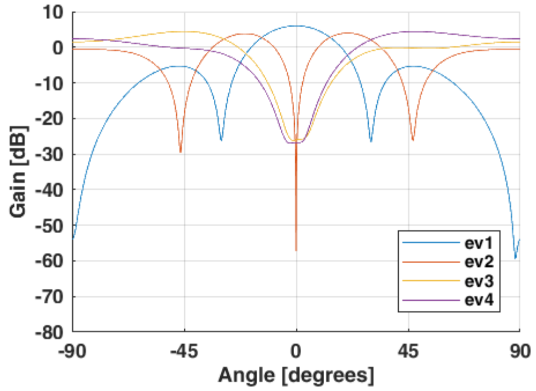

Figure 6.11: Directional sensitivity of the left singular vectors without interference filtering

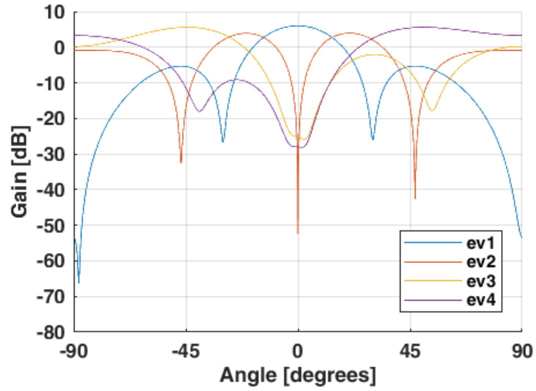

Figure 6.12: Directional sensitivity of the right singular vectors without interference filtering

6.2 Anechoic chamber

An artificial interferer can be created by using a Rhode & Schwarz signal generator. In addition to the receiver array and the transmitter array, a ninth antenna is placed in the anechoic chamber. This antenna is attached to the wall at an angle of approximately 70° with respect to the receiver array, see figure 6.13. Using this setup the spatial filter can be evaluated in a practical situation.

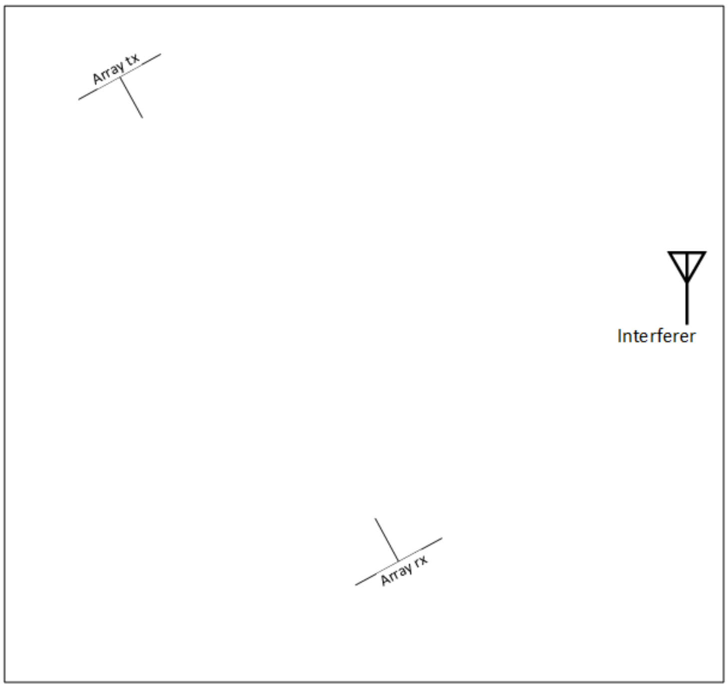

Figure 6.13: Direct path measurements with an interferer present.

Just like in the simulations, a profile is made with just the interferer present. The received signals are shown in figure 6.14. This figure shows that the amplitudes produced by antennas rx_3 and $rx4$ are significantly weaker than the ones produced by rx_1 and rx_2. The gains of the individual receiver channels were all set to 60dB, so it is unclear whether this is the result of shadowing effects, differences between the cables and antennas or due to some other cause. The goal of the experiment is to cancel the effects of this arbitrary interferer for which this signal is still suitable.

An interference profile is made to isolate the subspace of the interferer by calculating the eigenvalues and eigenvectors. Because of the shifts in phase and the changes in amplitude for the received signals of the interferer, it is unlikely that the MUSIC algorithm will indicate a clear and correct angle for the source of the interference. The resulting graph of the MUSIC algorithm in figure 6.16 indeed does not show a decisive angle. This is not really a problem as long as the eigenvalues and eigenvectors indicate a clear subspace for the interferer.

Table 6.6 shows that the fourth eigenvalue, the one that should correspond to the eigenvector spanning the signal subspace, is over a 100 times larger compared to the other eigenvalues. This indicates that the signal subspace of the interferer has been successfully isolated.

Using the determined eigenvectors the spatial filter $\mathbf{FF}^*$ is created. This filter is used to

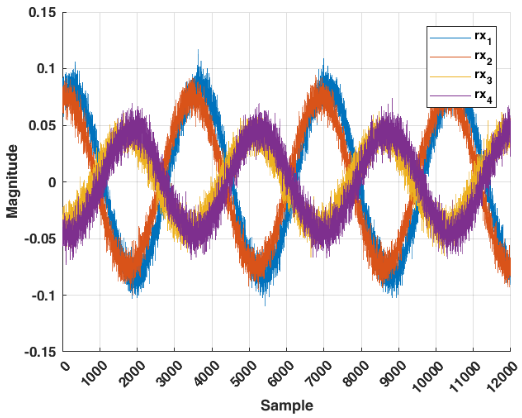

Figure 6.14: The interference signal as it is sampled by the receiver array.

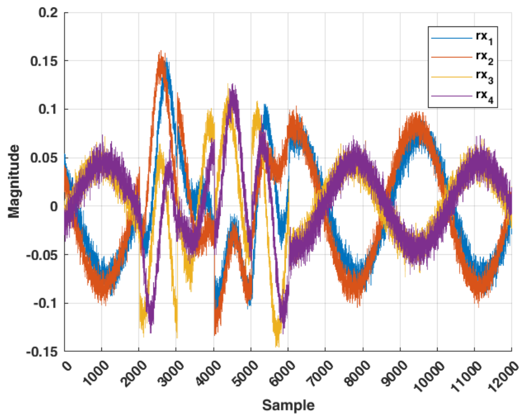

Figure 6.15: Sampled signals of the received pilot signal in the presence of an interferer.

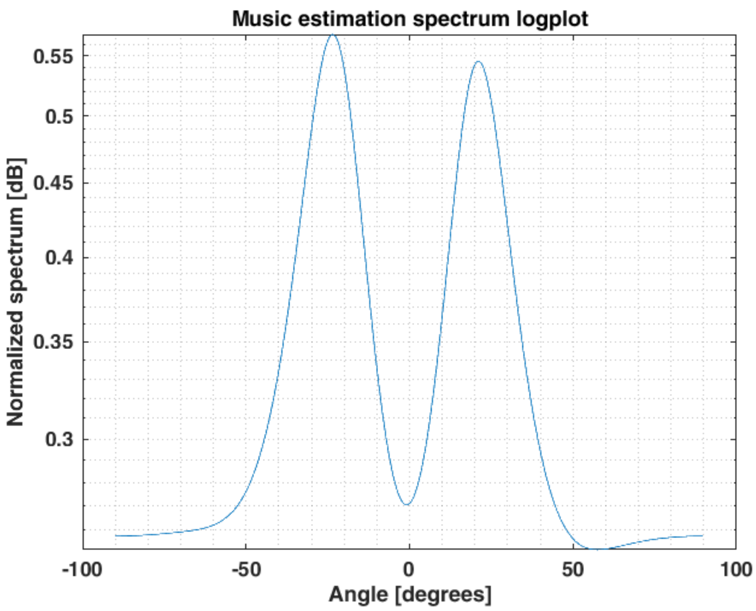

Figure 6.16: Results of the MUSIC algorithm using three noise subspace dimensions.

Table 6.6: Determined eigenvalues of the co-variance matrix of the calibration measurement.

0.0001	0	0	0
0	0.0001	0	0
0	0	0.0001	0
0	0	0	0.0166

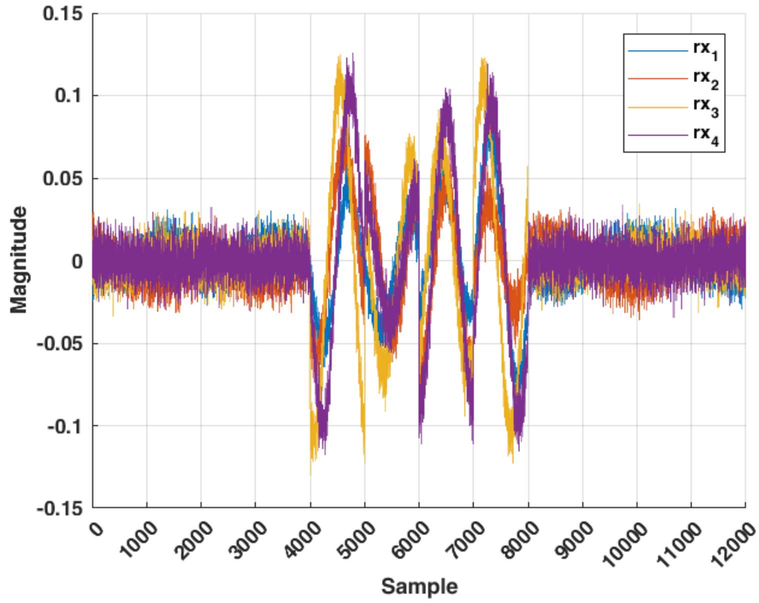

Figure 6.17: The received signals after multiplication with the spatial filter $\mathbf{FF}^*$.

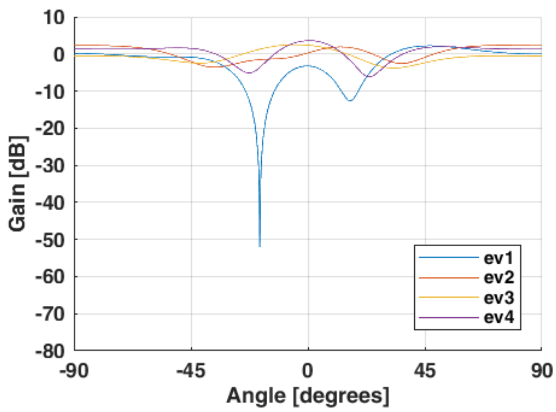

Figure 6.18: Angular sensitivity of the spatial filter $\mathbf{FF}^*$.

filter the interference of figure 6.15. The result of this filtering operation is shown in figure 6.17.

It is determined that most of the interference has been filtered out. In the simulations however, the interference was suppressed much more. The reason for the lack of performance can be found by looking at the angular sensitivity of the matrix used for filtering (figure 6.18). Because of the phase and amplitude differences in the interferer profile, it was expected that the directional sensitivity of the column vectors of the spatial filter would not show a null at the angle of incidence of the interferer (45°). Figure 6.18 not only shows that there indeed exists no such angle, but it also shows that the nulls of the filter show way less rejection than the ones encountered earlier. This would explain the deficit in the ability to suppress the interference.

Even though the interference suppression is not working as well as in simulations, it still has managed to suppress the interference by a factor 10 (in figure 6.17, the amplitude of the interference has been decreased from 0.08 to roughly 0.008 of the full scale voltage). This might improve even further if the issues with the phase offsets are resolved. These offsets may deteri-

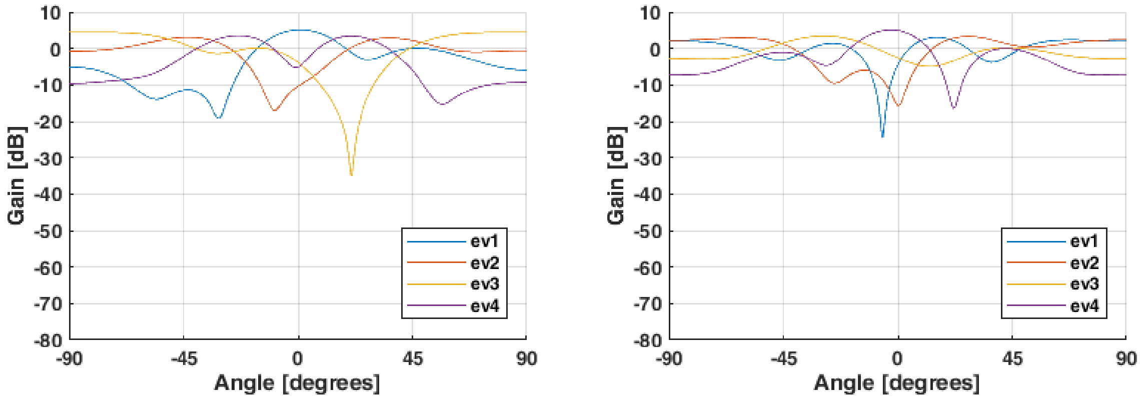

(a) Left singular vectors, **U**.

(b) Right singular vectors, **V***.

Figure 6.19: The directional sensitivity of the singular vectors for the experiment after filtering.

orate the rejection levels of the nulls and thus influence the performance of the filter.

To see how these operations affect the concepts of spatial multiplexing, the channel matrix is estimated using the filtered signals. Table 6.7 shows the singular values and figure 6.19 shows the directional sensitivity of the resulting singular vectors. Compared to the figures from table 5.8 these results are promising. The goal was to filter out the interferer without significantly affecting the other signals. The first three singular values show comparable numbers as the ones shown in table 5.8, indicating that the operation has not affected the operation of spatial multiplexing too much. The left singular vector corresponding to the strongest eigenvalue has a maximum gain at 0°, which inidicates that also the direct path has not been affected much.

Table 6.7: Singular Values and condition ratios of the simulation after filtering the received signals of the experiment.

	1	2	3	4
SV	0.2796	0.0592	0.0259	$6.5 \cdot 10^{-9}$
Ratio	1.0000	4.7220	10.779	$4.3 \cdot 10^{7}$

6.3 Conclusion

This chapter presented a technique by which interference could be filtered from the system by removing one of the available subspaces. This was done by taking a measurement with only the interferer present. The eigenvalues and eigenvectors of the captured signals were determined, which were used to construct a spatial filter. This filter was used to filter the interference from the training signals, taking the interference out of the equation for the channel estimation and the spatial multiplexing.

Although the correct operation of the filter was shown, no elaborate analysis had been performed on how the filter affects the signals concerning the spatial multiplexing operations. The results so far look promising, but more research on this part is required.

Chapter 7

Conclusion

Spatial multiplexing techniques have been presented in this project. These techniques have been tested in both simulations and practical experiments. In multiple scenarios the channel matrix has been successfully estimated using a least squares estimation. Singular value decompositions were performed on the channel matrices to obtain the singular values and the left- and right singular vectors. This research has shown how the singular values relate to the possible existence of spatial transmission paths. The singular vectors were analyzed by determining the directional sensitivity and the results were related back to the setup of the system. The found spatial transmission paths coincided to a large extent with the expected results. The found optimal spatial transmission paths include corrections for offsets in the system. Where possible, these offsets were taken into account during simulations and gave similar results to the ones observed during the experiments.

During the experiments it became clear that the performed measurements had some shortcomings. The fact that the synthesizers were not synchronous introduced phase offsets in the measurements. The proposed techniques automatically took these into account, making the results hard to interpret. In most measurements it was unknown in which signals a phase shift was introduced and how large this phase shift was. In some cases the experimental results could be verified by also introducing phase shifts to the simulations. In most cases however, the lack of calibrations in the antenna paths made it impossible to make justifiable statements.

Lastly, it has also been looked into how the system could be made more robust to interference. By doing a calibration measurement of the environment without the system's own transmitters active, a profile is made that provides information of the location of interfering sources. This profile was then successfully used to effectively cancel the interference in both simulations and the experiments. Although initial results looked promising, more research is required to see how the filtering of these signals affects the operations of spatial multiplexing.

Reflecting back on the goals of this project, the first three goals have successfully been achieved. A channel estimation algorithm was successfully implemented and by using a singular value decomposition, the optimal spatial transmission paths were found. For the last goal, being to investigate how the (spatial transmission) channels are affected by- and affect neighboring communication systems and how this can be reduced by looking at the interference footprint, good steps have been made. It has however not been completed as the issues concerning the coupling and the phase offsets took up most of the focus of this research.

Chapter 8

Future Work

During this research two issues stood out most. Firstly there were coupling effects observed on the receiver channels of the FMCOMMS5 board. This was ultimately resolved by broadcasting signals at very low power levels and using external amplifiers. Although this effectively solved the issue, it is still a mere workaround. This solution limited the setup to a frequency of 1400MHz, while the antennas were specified for 2.4GHz. It would be best to redo the experiments with a dedicated board for both transmitter and receiver. That way they are physically isolated and only then one can be completely sure that coupling is no longer an issue.

All the experiments were carried out in the assumption that the local oscillators of the receivers and transmitters were synchronized. During the processing of the results it became evident that this was not the case. Synchronized synthesizers would prevent phase offsets between the individual channels and would therefore make the results much more reliable. The device supports the feeding of an external local oscillator signal, that according to the documentation schematics, is fed to all the relevant synthesizers. Though the path length of these traces may still introduce phase offsets, at least this makes the offsets constant so they can be determined during calibrations and be accounted for.

The experiments were performed in two situations, the majority was performed inside an anechoic chamber, whilst the others were performed in a normal laboratory. In the first case all reflections are suppressed, whilst in the second they were quite dominant. It may be interesting to see how the techniques presented in this research perform in a situation that has characteristics of both. This could either be done in a large empty hall or on an open field. Using a sheet of absorbing material, it may also be possible to deduce where the reflections come from in a rich scattering environment and how these affect the system.

On the topic of channel estimation, this research made the assumption that the channel matrix was constant. This assumption was made because in literature the same assumption is commonly made. For application in real communication systems this assumption would not hold. A changing environment, people walking around the office for instance, will change the channel matrix. It is therefore required to make an estimation for the time interval for which this assumption holds to determine the required repetition interval of the channel estimation.

While analyzing the experiments, a lot of comparisons were done between the results of various setups. Even though the intention was to make these as comparable as possible, it is still likely that differences occurred. For instance, the measurements of the direct path with no array rotations were performed first. Afterwards, the measurements with a rotated array were done and only then the measurement was done that had no array rotations but did have an interferer present. This means that in between the interference and the no interference measurements, the array was rotated twice. It is likely that after rotating it back to 0°, it was still at a different angle than it was before. It could be beneficial to see how sensitive the system is to these kind of differences.

Because the issues with coupling and phase offsets took most up most of the time available for the experiments, the final goal of this research has not been treated as thoroughly as it deserved. It would be good to look further into the effects of the spatial filter on the operations of spatial multiplexing. Even more so if somehow the phase offsets would be resolved and the singular vectors could be analyzed better.

Bibliography

[1] John Litva and Titus K Lo. *Digital beamforming in wireless communications*. Artech House, Inc., 1996.

[2] Barry D Van Veen and Kevin M Buckley. Beamforming: A versatile approach to spatial filtering. *IEEE assp magazine*, 5(2):4–24, 1988.

[3] Moctar Mouhamadou, Patrick Vaudon, and Mohammed Rammal. Smart antenna array patterns synthesis: Null steering and multi-user beamforming by phase control. *Progress In Electromagnetics Research*, 60:95–106, 2006.

[4] C. E. Shannon. A mathematical theory of communication. *SIGMOBILE Mob. Comput. Commun. Rev.*, 5(1):3–55, January 2001.

[5] Mehrzad Biguesh and Alex B Gershman. Training-based mimo channel estimation: a study of estimator tradeoffs and optimal training signals. *IEEE transactions on signal processing*, 54(3):884–893, 2006.

[6] Bangjun Lei, Guangzhu Xu, Ming Feng, Ferdinand van der Heijden, Yaobin Zou, Dick de Ridder, and David MJ Tax. *Classification, parameter estimation and state estimation: an engineering approach using MATLAB*. John Wiley & Sons, 2017.

[7] John Hopcroft and Ravi Kannan. Foundations of data science. 2014.

[8] Andreas F Molisch. *Wireless communications*, volume 34. John Wiley & Sons, 2012.

[9] Rohde & Schwarz GmbH & Co KG. Assessing a mimo channel — - 8nt01 — rohde & schwarz, 2017.

[10] David Tse and Pramod Viswanath. *Fundamentals of wireless communication*. Cambridge university press, 2005.

[11] David A Belsley, Edwin Kuh, and Roy E Welsch. *Regression diagnostics: Identifying influential data and sources of collinearity*, volume 571. John Wiley & Sons, 2005.

[12] Charles Knapp and Glifford Carter. The generalized correlation method for estimation of time delay. *IEEE Transactions on Acoustics, Speech, and Signal Processing*, 24(4):320–327, 1976.

[13] Ralph Schmidt. Multiple emitter location and signal parameter estimation. *IEEE transactions on antennas and propagation*, 34(3):276–280, 1986.

[14] Yiheng Zhang, Dana H Brooks, Maria Angela Franceschini, and David A Boas. Eigenvector-based spatial filtering for reduction of physiological interference in diffuse optical imaging. *Journal of biomedical optics*, 10(1):011014, 2005.

[15] António, A-J van der Veen, and Geert Leus. Signal processing for communications. 2005.

[16] H. T. Friis. A note on a simple transmission formula. *Proceedings of the IRE*, 34(5):254–256, May 1946.

[17] Analog Devices Wiki. Ad9361 no-os software. https://wiki.analog.com/resources/eval/user-guides/ad-fmcomms2-ebz/software/baremetal, 2018.

[18] Analog Devices. Ad9361 (rev. f) datasheet. http://www.analog.com/media/en/technical-documentation/data-sheets/AD9361.pdf, 2016.

[19] Farnell. Delta7a/x/smam/rp/s/11 - hinged mount wifi / ism antenna. http://nl.farnell.com/siretta/delta7a-x-smam-rp-s-11/antenna-direct-mount-sma/dp/2666814.

[20] Comtest. Microwave chambers. http://www.comtest.eu/products/microwave-chambers.html.

[21] Comtest. Hybrid & microwave absorbers. http://www.comtest.eu/products/anechoic-chambers/absorbers.html.

[22] Analog Devices. Ad9361 (rev. f) reference manual ug-570. https://form.analog.com/Form_Pages/Catalina/CatalinaDesign.aspx?prodid=AD9361, 2017.

[23] RF Bay Inc. Lna 1440 10khz - 1400mhz low noise amplifier. http://rfbayinc.com/products_pdf/product_88.pdf, 2018.

[24] A Balanis Constantine et al. Antenna theory: analysis and design. *MICROSTRIP ANTENNAS, third edition, John wiley & sons*, 2005.

Acronyms

ADC Analog to Digital Converter

AoI Angle of Incidence

AWG Additive White Gaussian

CSI Channel State Information

csv comma separated file

DAC Digital-to-Analog

DOA Direction of Arrival

EM Electromagnetic

ENSM Enable State Machine

FSPL Free Space Path Loss

GUI Graphic User Interface

LNA Low Noise Amplifier

LO Local Oscillator

LoS Line of Sight

MSPS Mega Samples Per Second

MUSIC Multiple Signal Classification

MIMO Multiple Input Multiple Output

NF Noise Figure

OS Operating System

PCB Printed Circuit Board

RF Radio Frequency

RMS Root Mean Square

RSSI Received Signal Strength Indicator

SISO Single Input Single Output

SMA SubMiniature version A

SNR Signal to Noise Ratio

SVD Singular Value Decomposition

TIA Transimpedance Amplifier

UHF Ultra High Frequency

WGN White Gaussian Noise

Appendices

A ADI IIO Oscilloscope

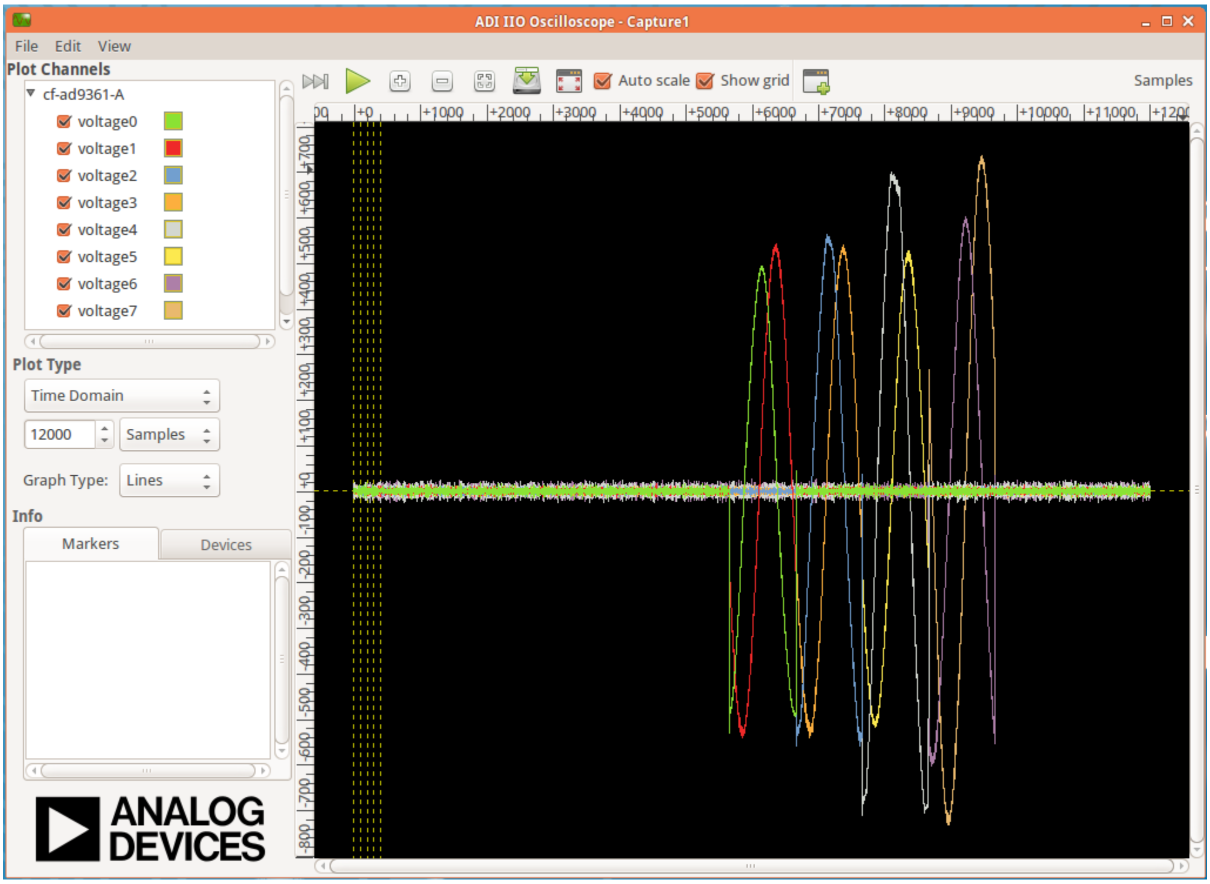

B Graphic User Interface Linux distribution

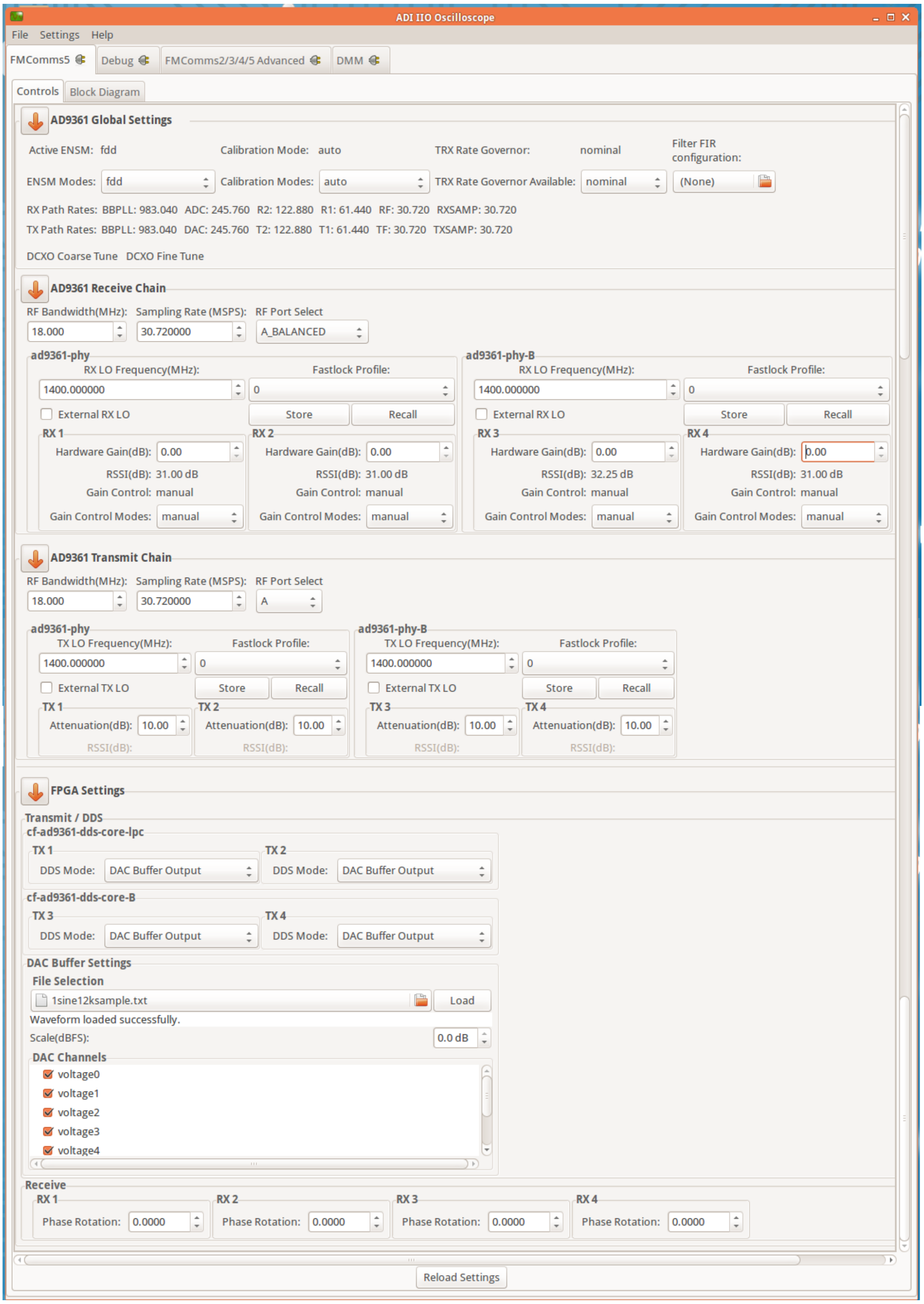

C Anechoic chamber